The Astrophysical Journal, 941:34 (24pp), 2022 December 10 https://doi.org/10.3847/1538-4357/ac8ea8

A Scintillation Arc Survey of 22 Pulsars with Low to Moderate Dispersion Measures

Dan R. Stinebring[1], Barney J. Rickett[2], Anthony H. Minter[3], Alex S. Hill[4,5], Adam P. Jussila[1,6], Lele Mathis[1,7], Maura A. McLaughlin[8,9], Stella Koch Ocker[1,10], and Scott M. Ransom[11]
[1] Department of Physics and Astronomy, 110 No. Professor St., Oberlin College, Oberlin, OH 44074, USA; dan.stinebring@oberlin.edu
[2] Department of Electrical and Computer Engineering, University of California, San Diego, CA 92093, USA
[3] Green Bank Observatory, P.O. Box 2, Green Bank, WV 24944, USA
[4] Department of Computer Science, Math, Physics, and Statistics, University of British Columbia, Kelowna, BC V1V 1V7, Canada
[5] Dominion Radio Astrophysical Observatory, Herzberg Astronomy & Astrophysics Research Centre, National Research Council, Penticton, BC, Canada
[6] Department of Bioinformatics and Systems Biology, 9500 Gilman Drive, Dept. 0419, University of California, San Diego, La Jolla, CA 92093-0419, USA
[7] Department of Chemistry, Northwestern University, 2145 Sheridan Rd, Evanston, IL 60208 , USA
[8] Department of Physics and Astronomy, West Virginia University, P.O. Box 6315, Morgantown, WV 26506, USA
[9] Center for Gravitational Waves and Cosmology, West Virginia University, Chestnut Ridge Research Building, Morgantown, WV 26505, USA
[10] Department of Astronomy and Cornell Center for Astrophysics and Planetary Science, Cornell University, Ithaca, NY 14853, USA
[11] National Radio Astronomy Observatory, 520 Edgemont Road, Charlottesville, VA 22903, USA
Received 2022 April 10; revised 2022 June 28; accepted 2022 June 28; published 2022 December 9

Abstract

Context. By providing information about the location of scattering material along the line of sight (LoS) to pulsars, scintillation arcs are a powerful tool for exploring the distribution of ionized material in the interstellar medium (ISM). Here, we present observations that probe the ionized ISM on scales of ∼0.001–30 au. *Aims.* We have surveyed pulsars for scintillation arcs in a relatively unbiased sample with DM < 100 pc cm^{-3}. We present multifrequency observations of 22 low to moderate DM pulsars. Many of the 54 observations were also observed at another frequency within a few days. *Methods.* For all observations, we present dynamic spectra, autocorrelation functions, and secondary spectra. We analyze these data products to obtain scintillation bandwidths, pulse broadening times, and arc curvatures. *Results.* We detect definite or probable scintillation arcs in 19 of the 22 pulsars and 34 of the 54 observations, showing that scintillation arcs are a prevalent phenomenon. The arcs are better defined in low DM pulsars. We show that well-defined arcs do not directly imply anisotropy of scattering. Only the presence of reverse arclets and a deep valley along the delay axis, which occurs in about 20% of the pulsars in the sample, indicates substantial anisotropy of scattering. *Conclusions.* The survey demonstrates substantial patchiness of the ionized ISM on both astronomical-unit-size scales transverse to the LoS and on ∼100 pc scales along it. We see little evidence for distributed scattering along most lines of sight in the survey.

Unified Astronomy Thesaurus concepts: Radio pulsars (1353); Interstellar medium (847); Interstellar scattering (854); Radio astronomy (1338); Radio spectroscopy (1359); Warm ionized medium (1788); Stellar wind bubbles (1635)

Supporting material: figure sets

1. Introduction

Nearly 55 yr after their discovery (Hewish et al. 1968), radio pulsars continue to be versatile probes of fundamental physics, plasma processes under extreme conditions, and the distribution of ionized gas in the Galaxy. Since early pioneering studies (Scheuer 1968; Rickett 1969, 1970), the unique wideband, pulsed character of the signal has been employed to explore the ionized component of gas along the line of sight (LoS) to these sources. With more than 3300 pulsars known (Manchester et al. 2005), they probe a wide range of distances and astrophysical conditions along sight lines and undergird the effort to develop a detailed model of the ionized gas distribution in the Milky Way (Cordes & Lazio 2002; Yao et al. 2017).

Classical studies of radio wave scintillation toward pulsars (e.g., Cordes et al. 1985; Cordes 1986; Gupta et al. 1994; Löhmer et al. 2001; Bhat et al. 2004; Kuzmin & Losovsky 2007) provided a broad-brush view of the scattering along many lines of sight and the tools to interpret it. In the study of interstellar scintillation (ISS), there has been an emphasis on measuring the characteristic bandwidth $\Delta\nu_{\rm iss}$ and timescale $\Delta t_{\rm iss}$ of the scintillation structure in two-dimensional dynamic spectra (DS; intensity as a function of radio frequency and time). This has yielded estimates of scattering angles toward pulsars, produced a better understanding of the distribution of scattering material along the LoS (Cordes & Rickett 1998), and also allowed the estimate of pulsar proper space velocities through the estimation of scintillation speeds (Cordes 1986; Gupta 1995).

However, the discovery that pulsar DS often have an underlying low-level modulation manifested as highly organized parabolic structures in the power spectrum of the DS (Stinebring et al. 2001) has provided a powerful new tool and uncovered several puzzles. The position of features in scintillation arcs can move on ∼week timescales or shorter (Hill et al. 2005; Wang et al. 2018), whereas the qualitative appearance of arcs can change on several month timescales (Stinebring et al. 2001; Main et al. 2020; Reardon et al. 2020, among others).

Scintillation arcs arise when the following conditions are met (Walker et al. 2004; Cordes et al. 2006): (a) scattering occurs in a relatively small fractional portion of the LoS (thin screen

condition), (b) the angular broadening function $B(\theta)$ has both a well-defined core and an outer halo; furthermore, the scintillation arc is enhanced and edge brightened if the angular image on the sky is highly anisotropic, particularly if it is roughly aligned along the effective velocity vector.

Most previous observational scintillation arc studies (e.g., Hill et al. 2003, 2005; Wang et al. 2005; Rickett et al. 2011; Bhat et al. 2016; Safutdinov et al. 2017; Wang et al. 2018; Stinebring et al. 2019; Reardon et al. 2020; Rickett et al. 2021; Yao et al. 2021; Chen et al. 2022; McKee et al. 2022) have focused on a relatively small number of well-observed pulsars and have explored a range of diverse scintillation arc phenomena. No prior study has explored the prevalence of scintillation arcs toward a sample of pulsars with fairly uniformly applied selection criteria. Since scintillation arcs often indicate the presence of highly organized linear scattering features toward pulsars—and since the astrophysical origin of those features is not known—it is of particular interest to characterize the frequency of occurrence of the arcs.

In addition to the work mentioned above, there has been a substantial amount of *precision* scintillation arc work—both interferometric and single-dish—in the past 10 yr or so. Much of this work was inspired by the remarkable interferometric study of PSR B0834+06 by Brisken et al. (2010), and work on interstellar holography (Walker & Stinebring 2005; Walker et al. 2008) laid important groundwork, too. Among other highlights in this scintillometry effort are several studies of binary pulsars (Rickett et al. 2014; Main et al. 2020; Mall et al. 2022), the detection of scattering from a supernova remnant around a pulsar (Yao et al. 2021), the location of multiple scattering screens toward nearby pulsars (Chen et al. 2022; McKee et al. 2022), and important new theoretical work (Simard et al. 2019a, 2019b; Sprenger et al. 2021; Shi & Xu 2021; Baker et al. 2022).

The remainder of the paper is organized as follows. In Section 2, we present the observations and our data processing methods. Section 3 focuses on secondary spectra production and the extraction of scintillation parameters from the data set. We briefly discuss the results from each of the 22 pulsars in Section 4, grouping them into three sets based on the prominence of scintillation arcs. Section 5 contains a detailed analysis of the observations and sets the results in a theoretical scattering context. We discuss the salient results in Section 6 and summarize the paper in Section 7. All data used in this paper are being made available as described in Section 2.4.

We have used the ATNF Pulsar Catalogue (PSRCAT) database[12] (Manchester et al. 2005) extensively throughout this work.

2. Observations and Data Processing

In this Scintillation Arc Survey (SAS), we studied scintillation arcs in 22 pulsars. The sources were chosen based on the following initial criteria: (i) visible with either the Green Bank Telescope (GBT) or Arecibo, (ii) DM < 50 pc cm^{-3}, and (iii) $S_{400} > 25$ mJy. Later in the project, we saw advantages to expanding DM coverage out to 100 pc cm^{-3} for at least several sources. We then included 6 pulsars visible from Arecibo in order to accomplish this. Because of Arecibo's sensitivity, we relaxed the flux density limit somewhat. See Table 1, which includes basic per-pulsar parameters such as source flux density, dispersion measure, transverse velocity, and previously measured scattering timescale.

[12] http://www.atnf.csiro.au/research/pulsar/psrcat, V1.67.

Table 1
Observational Parameters of the 22 Pulsars

PSR	S_{400} (mJy)	S_{1400} (mJy)	DM (pc cm^{-3})	Dist. (kpc)	$V_{\rm trans}$ (km s^{-1})
(1)	(2)	(3)	(4)	(5)	(6)
B0138+59	49	4.5	34.93	2.30	...
B0450+55	59	13	14.59	1.18	314.2
B0450–18	82	16.8	39.9	0.40	24.6
B0523+11	19.5	1.94	79.42	1.84	270.7
B0525+21	57	8.9	50.87	1.22	122.1
B0540+23	29	10.7	77.7	2.06[a]	217.2[a]
B0626+24	31	17.9[b]	84.18	3.00[b]	84.0[b]
B0628–28	206	31.9	34.42	0.32	77.3
B0809+74	79	10	5.75	0.43	102.7
B0818–13	102	6	40.94	1.90	405.2
B1508+55	114	8	19.62	2.10	962.6
B1540–06	40	15.2[b]	18.4[b]	3.11[b]	247.4[b]
B1706–16	47	14.5	24.89	0.56	125.3
B1821+05	18	1.7	66.78	2.00	51.1
B1857–26	131	15	37.99	0.70	170.3
B1907+03	21	1.5	82.93	2.86	...
B2021+51	77	27	22.55	1.80	107.8
B2045–16	116	22	11.46	0.95	510.1
J2145–0750	46	10.3	9	0.71	44.5
B2217+47	111	3	43.5	2.39	365.7
B2310+42	89	15	17.28	1.06	125.0
B2327–20	42	2.9	8.46	0.86	305.6

Notes. All values from the ATNF PSRCAT, v 1.67 unless indicated otherwise.
[a] Chmyreva et al. (2010).
[b] Deller et al. (2019).

In most cases, we obtained multifrequency DS at two epochs separated by less than a week. However, the GBT 1400 MHz observations were made 14 yr after those at the lower frequencies (Section 2.1).

Three data sets are employed in this paper, two from GBT and one from the Arecibo Observatory. They are described below. Observational details such as epoch of observation, center frequency, and bandwidth are given in Table 2.

2.1. GBT Observations

The observations in the first and largest portion of the data set were made with the Robert C. Byrd GBT between 2005 September 17–24. For each of the 16 GBT sources, a 60 minutes DS was obtained with a 10 s dump time of the Spectral Processor spectrometer. We used the Spectral Processor in a mode that produced $N_{\rm chans} = 1024$ across a bandwidth ranging from 5 to 40 MHz in binary steps. The center frequencies of the two bands were 340 and 825 MHz. Each front-end receiver was mounted at the prime focus, and only one front end could be mounted at a time. Initial observations were made at 340 MHz for the two days followed, five days later, by observations for two days with the 825 MHz receiver in place.

Another set of GBT observations, centered at 1400 MHz, was made during the period 2020 January–April. DS were obtained for 13 of the pulsars in the sample at this frequency, with the frequency range chosen to minimize the radio frequency interference (RFI) based on diagnostic scans performed with the GBT. All observations used the VEGAS spectrometer with 8192 spectral channels across 100 MHz

Table 2
Details of the Observations

#	PSR	Telescope	Center Freq. (MHz)	Bandwidth (MHz)	Nchans[a]	MJD
(1)	(2)	(3)	(4)	(5)	(6)	(7)
1	B0138+59	GBT	340	5	1024	53630
2	B0138+59	AO	825	40	1024	53637
3	B0450+55	GBT	340	5	1024	53632
4	B0450+55	GBT	825	40	1024	53637
5	B0450+55	GBT	1400	100	512	58920
6	B0450-18	GBT	340	5	1024	53632
7	B0450-18	GBT	824	40	1024	53637
8	B0450-18	GBT	1400	100	1024	58913
9	B0523+11	AO	422	2	4096	58132
10	B0523+11	AO	1450	160	4096	58131
11	B0525+21	AO	1390	40	4096	58131
12	B0540+23	AO	431	10	4096	58130
13	B0540+23	AO	1450	160	4096	58130
14	B0626+24	AO	431	10	4096	58132
15	B0626+24	AO	1390	40	4096	58133
16	B0628-28	GBT	340	5	1024	53632
17	B0628-28	GBT	825	40	1024	53637
18	B0628-28	GBT	1400	100	1024	58904
19	B0809+74	GBT	340	5	1024	53630
20	B0809+74	GBT	832	24	251	53637
21	B0809+74	GBT	1400	100	1024	58877
22	B0818-13	GBT	340	5	1024	53632
23	B0818-13	GBT	824	40	1024	53637
24	B0818-13	GBT	1400	100	1024	58920
25	B1508+55	GBT	340	5	1024	53632
26	B1508+55	GBT	825	20	1024	53637
27	B1508+55	GBT	1400	100	1024	58933
28	B1540-06	GBT	340	5	1024	53630
29	B1540-06	GBT	825	40	1024	53634
30	B1540-06	GBT	1400	100	1024	58964
31	B1706-16	GBT	340	5	1024	53630
32	B1706-16	GBT	824	40	1024	53634
33	B1706-16	GBT	1400	100	1024	58965
34	B1821+05	AO	431	10	4096	58132
35	B1857-26	GBT	340	5	1024	53631
36	B1857-26	GBT	824	40	1024	53635
37	B1907+03	AO	1470	40	4096	58131
38	B2021+51	GBT	340	5	1024	53632
39	B2021+51	GBT	824	40	1024	53637
40	B2021+51	GBT	1400	100	1024	58922
41	B2045-16	GBT	340	5	1024	53631
42	B2045-16	GBT	824	40	1024	53635
43	B2045-16	GBT	1400	100	1024	58922
44	J2145-0750	GBT	340	5	1024	53631
45	J2145-0750	GBT	825	40	1024	53635
46	B2217+47	GBT	340	5	1024	53632
47	B2217+47	GBT	825	40	1024	53637
48	B2217+47	GBT	1400	100	1024	58920
49	B2310+42	GBT	340	5	1024	53632
50	B2310+42	GBT	825	40	1024	53637
51	B2310+42	GBT	1400	100	1024	58874
52	B2327-20	GBT	340	5	1024	53632
53	B2327-20	GBT	824	40	1024	53637
54	B2327-20	GBT	1400	100	256	58877

Note.
[a] Number of frequency channels. The GBT 1400 MHz data were taken with 8192 channels and downsampled.

bandwidth, and spectra were written out every 10 s. These observations were made ≈15 yr later than those for the low-frequency GBT data. Although the 1400 MHz data shed important light on the scintillation arc structure seen at lower frequencies, care is needed in comparing features at widely separated epochs.

2.2. Arecibo Observations

Observations were made with the William E. Gordon Arecibo Telescope between 2018 January 12–15. Six pulsars were observed, three at the dual frequencies of 430 and 1450 MHz. Successful observations of the other three were only possible at a single frequency, either 430 or 1450 MHz. The Mock spectrometers were used for the observations, and the bandwidths ranged between 2 and 160 MHz, all with 4096 frequency channels and a 10 s interval between accumulated spectra.

2.3. Data Processing

DS were formed in the following fashion, similar to that done by Hill et al. (2003). Data were binned into a three-dimensional cube: pulse phase, radio frequency, and subintegration number (or time; 10 s per time slice). The cube was then collapsed along the pulse phase axis in order to locate the pulse. An ON pulse window was established, by eye, that contained more than 95% of the pulse energy. For these pulsars, the ON window was typically about 5%–10% of the total pulse period. An OFF pulse region of the same size was then identified from the cumulative pulse profile. The DS was formed from each subintegration by calculating

$$S_i(\nu) = \frac{\mathrm{ON}_i(\nu) - \mathrm{OFF}_i(\nu)}{\langle \mathrm{OFF}(\nu) \rangle}, \quad (1)$$

where ν is the radio frequency, $\langle \mathrm{OFF}(\nu) \rangle$ represents the average off-pulse spectrum (the bandpass), i indexes the subintegrations, and the division by this denominator partially corrects for the varying sensitivity across the band.

When we substitute t for time (0–60 m in 10 s increments) in place of the subintegration number and ν is also discrete, the DS will be denoted as $S(t, \nu)$ as displayed, for example, in the upper panels of Figure 1. Because of the location of the GBT in the National Radio Quiet Zone and the differential (ON–OFF) nature of the spectrum formation, RFI was not a major problem in the analysis. Arecibo observations were more strongly affected by RFI, and the GBT—1400 MHz observations also had persistent RFI in several channels slightly below 1420 MHz.

For many of our DS observations there are deep amplitude modulations due to broadband intrinsic pulsar variability such as nulling. Nulls appear as brief minima, which are often near zero amplitude, and last only one time step for most pulsars. We estimate this by averaging $S(t, \nu)$ over frequency at each 10 s time step to obtain the pulsed time series $p(t)$. As we describe below, we subtract the estimated $p(t)$ from $S(t, \nu)$ at each time step, in order to minimize its effect on the secondary spectrum (SS).

The SS is the primary data product of interest in the study, computed from the power spectrum of the DS. Cordes et al. (2006) refer to this quantity as $S_2(f_t, f_\nu) = |\tilde{S}_c(t, \nu)|^2$, where the tilde denotes a Fourier transform, and the axes f_t and f_ν are conjugate to the t and ν axes, respectively. However, it has become more common in the literature to identify f_t with differential Doppler frequency, f_D, and the conjugate frequency axis, f_ν, with differential delay, τ. We use that notation in what follows. An example of $S_2(f_D, \tau)$ is shown in Figure 1 as well, where we follow the convention, standard in this field, of displaying S_2 using a logarithmic gray scale in order to encompass the large dynamic range often present in the data. Note that the color table for the display of S_2 depends sensitively on the upper and lower power limits displayed. We comment further on this in the caption to Figure 1.

As noted above, intrinsic pulsar variations $p(t)$ modulate $S(\nu, t)$ coherently across the entire bandwidth. Hence they contribute power to the SS along the f_D axis $S_2(f_D, \tau = 0)$, which is set to zero by subtracting $p(t)$. S_2 is computed via a finite discrete Fourier transform, and there is a corresponding spectral response function in delay and Doppler, whose sidelobes can allow leakage of power from isolated peaks to spread through the SS. By subtracting the intrinsic $p(t)$ from the DS, we reduce the corresponding leakage to higher delays. We further reduce leakage of power from the peak near the origin of S_2 by applying a window function to the DS. We use a cosine-squared window to taper the outer 20% of the DS to zero in both time and frequency.

2.4. Data Availability

The DS analyzed in this paper can be accessed at DOI: 10.5281/zenodo.6413233. Machine-readable versions of the tables, including substantially more information in the case of Table 3, are available at the same digital object identifier (DOI). The software used to analyze and display the data is not in a public repository. Any questions related to the details of the processing or access to the software employed should be directed to one of the first two authors.

3. Secondary Spectrum—Data Presentation

We have assembled the 54 observations of the 22 pulsars as a figure set visible online. In each plot, we show the DS and associated secondary spectra together with two lower panels as described below. Of these, 13 pulsars were observed at three frequencies, 6 at two frequencies, and 3 were observed at one frequency only.

Examples of the display format are shown in Figure 1, where we show data for 3 of the 22 pulsars in the data set. In these cases, data are available at frequencies of 340, 825, and 1400 MHz. In each case, the upper panel is the DS in standard gray-scale format with linear scaling. The lower panel shows the SS with decibel scaling chosen to emphasize the structure at low levels (ranging from white at the mean noise level S_{noise} and saturating at black at a level 5 dB below its global maximum). S_{noise} is estimated from the mean of S_2 in a rectangular region away from areas of ISS, which is outlined in green.

Also shown at the lower left of each plot is the autocorrelation function (ACF) of the DS versus offsets in time and frequency. Cuts along the axes are used to estimate the decorrelation times and bandwidths, as described in more detail in Section 5.1. The displayed range is set to be 5 times wider in both coordinates. Lower right panels in each plot, discussed in Section 5.3, show how we estimate the curvature of any parabolic arc structure present.

3.1. Overview

The 54 plots provide a visual description of the ISS. As has long been known, the scintillation appears as a random distribution of peaks in the DS, whose widths in frequency and time can be characterized from its ACF. Some such peaks (*scintles*) can appear tilted causing tilts in the ACFs. In traditional studies of ISS, the ACF widths are the main

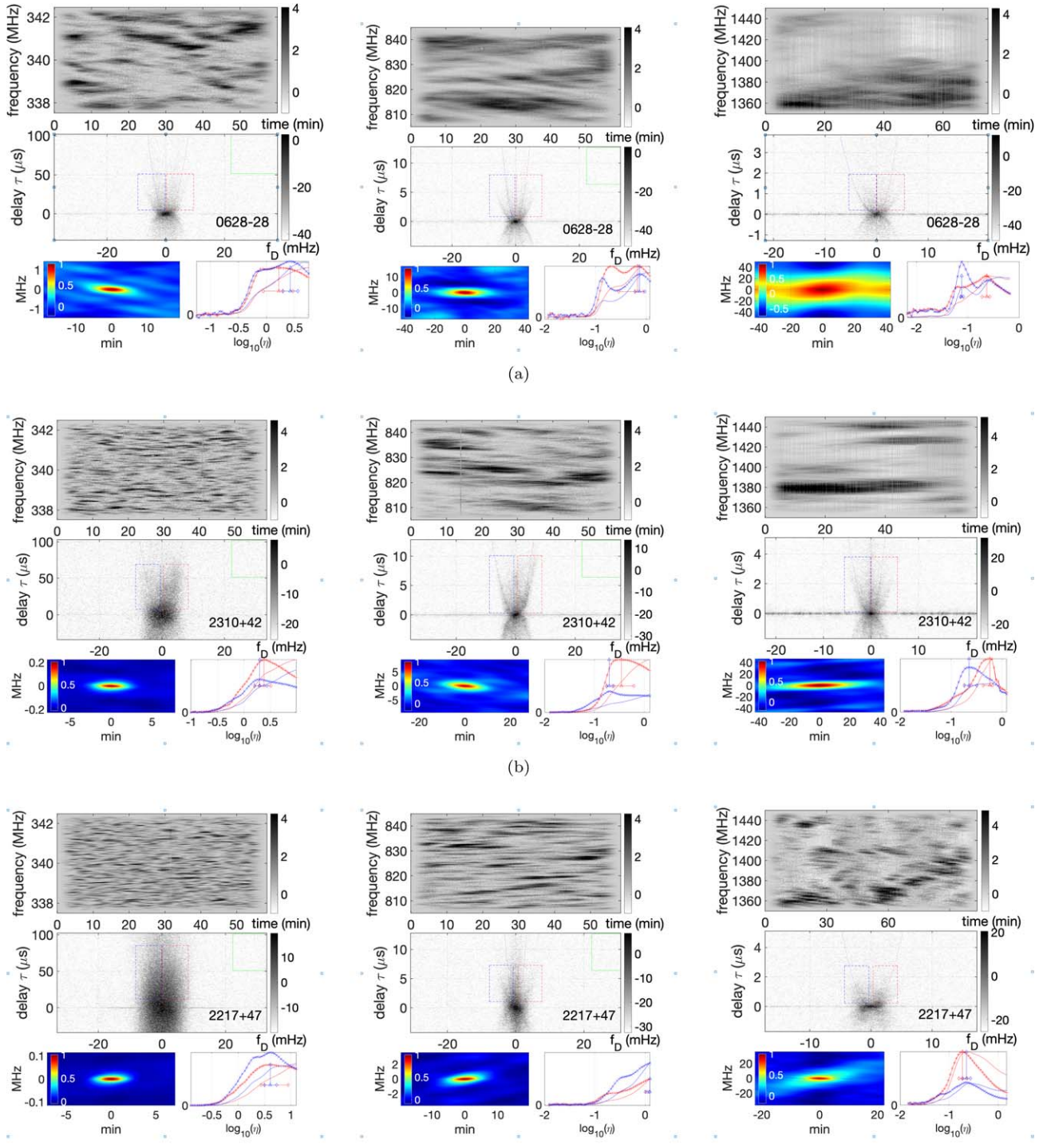

Figure 1. Sample of main data display for pulsar B0628–28 (a), dynamic and secondary spectra for B2310+42 (b), and B2217+47 (c). *Left column*: 340 MHz. *Middle column*: 820 MHz. *Right column*: 1400 MHz. In each row, the upper panels are dynamic spectrum linearly scaled in units of the mean flux density; middle panels are secondary spectra S_2 with decibel scaling. Lower left panels are autocorrelations of the dynamic spectra vs. time lag (horizontal, minutes) and frequency lag (vertical, MHz). The lower right panels show curvature estimation by parabolic summation of S_2 over a range in delay (defined by the blue and red rectangles in S_2). The summation is plotted vs. log of curvature η; all of the parabolas have apexes at the origin. As described in Section 5.3, the plain red and blue curves plot the direct linear summations for negative and positive f_D, and the curves with x marks are summations weighted by $|f_D|$. The locations of the peaks in the weighted curves are flagged by vertical lines with a horizontal bar defining a width at 0.95 of the peak. Faint dotted red and blue parabolas are overplotted on the SS at these estimated curvatures. The complete figure set (54 images spanning 22 pulsars) is available in the online journal.

(The complete figure set (22 images) is available.)

Table 3
Analysis of Dynamic and Secondary Spectra

#	PSR	Freq. (MHz)	MJD	$\Delta\nu_{\rm iss}$ (MHz)	$\pm\Delta\nu_{\rm iss}$ (MHz)	$\Delta t_{\rm iss}$ (s)	$\pm\Delta t_{\rm iss}$ (s)	$\eta_{\rm p,l}$ (s^3)	$\eta_{\rm p}$ (s^3)	$\eta_{\rm p,u}$ (s^3)	$\eta_{\rm edge}$ (s^3)	S/N	$S/N_{\rm iss}$	$\eta_{\rm cred}$	$s_{\rm max}$	Arc Power Asym., κ
(1)	(2)	(3)	(4)	(5)	(6)	(7)	(8)	(9)	(10)	(11)	(12)	(13)	(14)	(15)	(16)	(17)
1	B0138+59	340	53630	0.0253	0.00681	495	131	⋯	⋯	⋯	8.27	0.325	17.6	0	⋯	0.319
2	B0138+59	825	53637	0.98	0.737	847	637	⋯	⋯	⋯	1	0.61	49.2	0	⋯	–0.186
3	B0450+55	340	53632	0.129	0.0383	123	36.7	⋯	⋯	⋯	0.112	1.69	65	0	0.514	–0.662
4	B0450+55	825	53637	2.85	2.04	257	183	0.214	0.259	0.296	0.0204	3.26	37.5	1	0.766	–0.207
5	B0450+55	1400	58920	9.6	7.24	367	277	0.0489	0.0533	0.061	0.0384	10.8	3930	1	0.66	0.566
6	B0450–18	340	53632	0.00756	0.000536	70.9	4.27	2.77	3.55	5.41	1.79	4.99	30.8	2	0.136	0.0157
7	B0450–18	825	53637	0.151	0.0178	121	13.9	0.703	0.797	0.904	0.624	8.13	71.5	2	0.173	–0.127
8	B0450–18	1400	58913	9.7	11.5	1140	1350	1.53	1.79	2.15	1.11	57.9	8830	2	0.575	–0.34
9	B0523+11	422	58132	0.000588	7.56×10^{-6}	⋯	⋯	⋯	⋯	⋯	0.264	0.071	1.06	0	0.697	–0.286
10	B0523+11	1450	58131	0.0697	0.002	39.7	1.03	0.101	0.123	0.148	0.0302	0.385	2.54	1	0.695	–0.468
11	B0525+21	1390	58131	0.105	0.00457	20.9	0.999	0.0414	0.0468	0.0533	0.0327	1.58	9.28	1	0.198	0.451
12	B0540+23	432	58130	0.0032	6.61×10^{-5}	13.6	0.278	⋯	⋯	⋯	0.0945	0.563	2.94	0	0.202	–0.336
13	B0540+23	1450	58130	0.234	0.0129	47.7	2.65	0.0349	0.0415	0.0493	0.0215	14.5	74.6	1	0.255	–0.857
14	B0626+24	432	58132	0.00365	0.000144	81.9	2.71	7.83	10.2	14.4	3.36	1.39	11	1	0.506	0.507
15	B0626+24	1390	58133	0.288	0.0676	200	47	0.905	1.29	1.69	0.568	0.275	27.9	1	0.573	0.363
16	B0628–28	340	53632	0.145	0.0621	228	98.1	1.41	2.16	3.29	0.467	7.02	74.7	1	0.509	–0.0623
17	B0628–28	825	53637	1.68	1.36	559	452	0.442	0.702	0.899	0.113	19	185	1	0.665	0.086
18	B0628–28	1400	58904	12.9	23.3	1150	2090	0.132	0.156	0.175	0.0504	30.8	6040	1	0.559	–0.145
19	B0809+74	340	53630	0.413	0.532	691	889	1.34	1.45	1.64	0.0792	1.52	65.5	1	0.478	–0.00856
20	B0809+74	833	53637	1.4	1.16	294	242	⋯	⋯	⋯	0.0136	0.0765	6.58	0	0.501	–0.257
21	B0809+74	1400	58877	9.28	11.7	762	961	⋯	⋯	⋯	0.0244	0.417	856	0	0.523	0.137
22	B0818–13	340	53632	⋯	⋯	78.2	3.47	⋯	⋯	⋯	2.67	2.86	22.1	0	0.937	–0.0529
23	B0818–13	825	53637	0.0775	0.0101	224	25.9	⋯	⋯	⋯	2.53	33.1	435	0	0.984	–0.131
24	B0818–13	1400	58920	2.26	0.85	333	125	0.197	0.287	0.451	0.104	16.8	2060	1	0.915	0.151
25	B1508+55	340	53632	0.0193	0.00154	51	4.03	1.07	1.45	1.77	0.794	26.2	101	2	0.943	–0.359
26	B1508+55	825	53637	0.449	0.1	92.2	20.7	0.185	0.207	0.229	0.145	3.3	13.9	2	0.932	–0.84
27	B1508+55	1400	58933	8.77	4.99	234	133	0.0504	0.0579	0.0662	0.0353	7.79	736	2	0.918	–0.139
28	B1540–06	340	53630	0.0199	0.00181	68.5	6.13	1.66	1.95	2.33	0.981	2.38	12	2	0.506	–0.146
29	B1540–06	825	53634	0.35	0.0598	118	20.1	0.284	0.319	0.363	0.231	9.19	60.8	2	0.496	–0.149
30	B1540–06	1400	58964	10.9	14.7	1010	1350	⋯	⋯	⋯	0.239	0.92	1150	0	0.915	0.203
31	B1706–16	340	53630	0.0664	0.0235	342	121	⋯	⋯	⋯	1.32	2.03	105	0	0.943	0.0385
32	B1706–16	825	53634	1.68	1.32	536	420	1.54	1.76	3.02	0.762	18.9	626	1	0.882	–0.403
33	B1706–16	1400	58965	5.28	4.7	934	830	⋯	⋯	⋯	0.46	14.6	19000	0	0.894	0.077
34	B1821+05	432	58132	0.0298	0.00288	103	9.99	⋯	⋯	⋯	0.888	0.4	22	0	0.123	0.0697
35	B1857–26	340	53631	0.00152	9.58×10^{-5}	7.82	0.239	⋯	⋯	⋯	0.0258	0.129	0.664	0	0.0721	–0.0731
36	B1857–26	825	53635	0.0134	0.000873	12.5	0.341	⋯	⋯	⋯	0.00522	2.52	12.9	0	0.167	–0.235
37	B1907+03	1470	58131	0.046	0.00176	27.2	1.08	0.121	0.171	0.193	0.0394	0.0938	2.69	1	⋯	0.124
38	B2021+51	340	53632	0.154	0.072	251	117	⋯	⋯	⋯	1.03	3.29	80.2	0	0.353	–0.00716
39	B2021+51	825	53637	1.32	0.762	363	210	0.825	1.19	1.45	0.21	36.8	1040	1	0.537	–0.134
40	B2021+51	1400	58922	11.5	17.3	1230	1850	0.116	0.13	0.141	0.0941	69.1	8510	2	0.267	–0.0643
41	B2045–16	340	53631	0.306	0.127	101	42.1	0.109	0.122	0.136	0.0519	6.75	96.5	1	0.461	–0.0557
42	B2045–16	825	53635	4.05	3.12	215	166	0.0175	0.0192	0.0208	0.0145	3.72	66.3	2	0.442	–0.292
43	B2045–16	1400	58922	10.8	8.1	312	234	0.00684	0.00752	0.00844	0.00558	13.4	2320	2	0.473	0.115
44	J2145–0750	340	53631	0.218	0.173	523	416	⋯	⋯	⋯	1.51	0.0553	19.7	0	0.378	–0.234
45	J2145–0750	825	53635	1.6	1.08	407	274	1.13	1.32	1.46	0.0539	0.0196	8.59	1	0.309	–0.262
46	B2217+47	340	53632	0.0104	0.000859	84.8	6.39	⋯	⋯	⋯	1.45	38.3	279	0	0.854	–0.13

Table 3
(Continued)

#	PSR	Freq. (MHz)	MJD	$\Delta\nu_{\rm iss}$ (MHz)	$\pm\Delta\nu_{\rm iss}$ (MHz)	$\Delta t_{\rm iss}$ (s)	$\pm\Delta t_{\rm iss}$ (s)	$\eta_{\rm p,l}$ (s^3)	$\eta_{\rm p}$ (s^3)	$\eta_{\rm p,u}$ (s^3)	$\eta_{\rm edge}$ (s^3)	S/N	$S/N_{\rm iss}$	$\eta_{\rm cred}$	$s_{\rm max}$	Arc Power Asym., κ
(1)	(2)	(3)	(4)	(5)	(6)	(7)	(8)	(9)	(10)	(11)	(12)	(13)	(14)	(15)	(16)	(17)
47	B2217+47	825	53637	0.357	0.0878	233	56.9	1.04	1.24	1.24	0.168	7.9	90.3	0	0.913	–0.229
48	B2217+47	1400	58920	3.61	1.42	266	105	⋯	⋯	⋯	0.078	3.09	531	1	0.834	0.404
49	B2310+42	340	53632	0.0219	0.00245	92.6	10.1	1.78	2.19	3.01	1.2	4.04	35.9	1	0.454	0.232
50	B2310+42	825	53637	0.941	0.447	337	160	0.204	0.274	0.434	0.151	10.9	79	1	0.379	0.433
51	B2310+42	1400	58874	4.66	5.02	1050	1140	0.303	0.4	0.485	0.228	104	10000	1	0.72	0.0898
52	B2327–20	340	53632	0.34	0.2	184	108	0.993	1.09	1.19	0.556	0.298	13.4	2	0.752	–0.786
53	B2327–20	825	53637	1.75	0.805	177	81.5	0.18	0.186	0.194	0.0878	0.0481	4.78	2	0.753	0.116
54	B2327–20	1400	58877	7.93	7.02	431	382	⋯	⋯	⋯	0.0551	0.707	1310	0	0.955	0.0452

Note. Three values are given for η from the parabolic summing algorithm: a lower bound ($\eta_{\rm p,l}$), the most likely value ($\eta_{\rm p}$), and an upper bound ($\eta_{\rm p,u}$). $\eta_{\rm edge}$ is the point of maximum slope in the parabolic summing curve. S/N is, in the DS, the ratio of the signal variance to the noise variance. $S/N_{\rm iss}$ is a similar quantity, but with the signal variance calculated in the DD box (see Section 5.3.2). $s_{\rm max}$ is the estimate of primary screen location (maximum distance from the pulsar; see Equation (11)). The arc power asymmetry is $\kappa \equiv (R - L)/(R + L)$, where R is the parabolic summation on the rhs ($f_D > 0$), and L is the corresponding power on the lhs of the parabola. Columns (6) and (8) are finite scintle estimates of the uncertainty in $\Delta\nu_{\rm iss}$ and $\Delta t_{\rm iss}$, respectively. See text for details.

parameters extracted from an observation, and ISS was originally recognized by the narrowing in the ISS bandwidth for pulsars at increasing DM (Rickett 1970).

Scintillation arcs were discovered as systematic curved structures in $S_2(\tau, f_D)$, often many decibels below the peak. The commonest form of arc is a simple *forward parabolic arc* $\tau = \eta f_D^2$, with its apex at or near the origin, as characterized by its curvature (η). In general we define arcs by secondary spectra that are peaked narrowly (or broadly) about such a parabola. Such arcs can exhibit a dip or *valley* along the delay axis near zero f_D; for example, see B0450–18 at 340 MHz (Figure 1.3).

Multiple forward arcs have been reported from some nearby pulsars: e.g., Putney & Stinebring (2006; pulsars B0329+54, B0823+26, B0919+06, B1133+16, B1642–03, and B1929+10); McKee et al. (2022; B1133+16); and Reardon et al. (2020; J0437-4715). However, there are only a few examples in the observations reported here, which include many more distant pulsars. In Figure 1(a) for B0628–28 at 825 MHz, the outer arc provides a relatively sharp boundary with little SS power outside, while the inner arc is much-less distinct. A second example is B2021+51 at 1400 MHz in Figure 1.17. A third example is B2310+42 at 825 MHz in Figure 1(b). It shows an outer arc, which also acts as a sharp boundary, which we call a *bounding arc*. The inner structure is more like a broad ridge than an arc. Note also that at 340 MHz the outer arc no longer acts as a sharp boundary. Similar differences between low and high frequencies are common throughout the survey data and are discussed further in Section 4. For B2310+42 we also show results at 1400 MHz, which we discuss in Section 4.

A number of pulsars exhibit isolated peaks, which may or may not lie near a forward parabolic arc. When such peaks follow a curved shape, we refer to them as *reverse arclets*, which were discovered in pulsar B0834+06 (Hill et al. 2003). Reverse arclets have negative curvature and apexes that lie close to the underlying forward arc. Figure 1.3 shows similar reverse arclets for B0450–18, which we have analyzed in detail elsewhere (Rickett et al. 2021). Another example can be seen in Figure 1.5 for B0525+21. Reverse arclets can be understood as the interference of scattering from a discrete offset point with a central anisotropic scattered distribution (Walker et al. 2004; Cordes et al. 2006). Their apexes lie on the forward arc when the offset point lies along the axis of anisotropy. Their curvature equals the reverse of the forward arc when the scattering is localized in the same screen as the main forward arc. This situation can sometimes be recognized when a reverse arclet extends inwards as far as zero f_D and passes through the origin. Arclets with forward curvature are rare.[13] Pulsar B1508+55 exhibits an unusual variation of *flat arclets* at 825 and 1400 MHz (Figure 1.11). In another variation, Figure 1.2 for B0450+55 shows an isolated point in its SS, which is not extended in f_D.

Another common feature is *asymmetry* in the intensity of S_2 versus differential Doppler f_D, which appears as *tilted* scintles in the DS and a tilted ACF.[14] Asymmetry can also be seen between the height of the positive and negative peaks in the parabola-summation curves. There may also be asymmetry in that the apex of an arc may be slightly offset to positive or negative f_D, which can be due to refraction by a transverse gradient in the electron distribution somewhere along the LoS (Cordes et al. 2006).

Scintillation arc studies hold the promise of being able to locate scattering material along the LoS, at least in optimal cases. Dating back to the earliest days of ISS studies, the prevailing paradigm has been one of a pervasive turbulent medium punctuated by *clouds* of increased turbulence along the LoS. For example, see Cordes et al. (1991). Although there is no thorough analysis of how distributed scattering along the LoS will show up in the SS, several lines of argument indicate that it should produce a *centrally concentrated* (CC) region of power around the origin. An example of an SS that displays this distribution is shown in the left panel of Figure 1(c). The DS in this case consists of a large number of scintles with no evidence for within a scintle. Referring to the two higher-frequency observations for this pulsar in the center and right panels, we see that the scintle structure broadens out with increased intra-scintle modulation in the DS and a corresponding tendency toward arc-like behavior in the SS. We will discuss this generic frequency development further in Section 5.5.

3.2. Basic Scintillation Parameters

3.2.1. ISS Decorrelation Widths

As is the conventional procedure (e.g., Cordes et al. 1985; Gupta et al. 1994), we estimated the frequency scale, $\Delta\nu_{\rm iss}$, and the timescale, $\Delta t_{\rm iss}$, of the scintillation structure using the intensity ACF, $R(\nu, t)$, which we discuss in more detail in Section 5.1. These decorrelation scales are obtained, respectively, by determining where $R(\Delta\nu_{\rm iss}, 0) = 0.5\,R(0, 0)$ and $R(0, \Delta t_{\rm iss}) = 0.5\,R(0, 0)$ and are presented in Table 3. (We note that this definition differs from the convention of Rickett 1970 and Cordes 1986, where the e^{-1} point is used in the autocorrelation time lag). The fractional errors in them are estimated as $N_{\rm iss}^{-1/2}$, where $N_{\rm iss}$ the number of independent ISS fluctuations over the observed bandwidth (B) and time span (T). We define $N_{\rm iss} \approx (\epsilon B/2\Delta\nu_{\rm iss})(\epsilon T/2\Delta t_{\rm iss})$, since $\Delta\nu_{\rm iss}$ and $\Delta t_{\rm iss}$ are half widths of the autocorrelations, and where $\epsilon = 0.2$ accounts for the fact that the exponentially distributed intensity of the scintles leads to peaks in ISS that are sparsely distributed in time and frequency resulting in fewer independent ISS fluctuations (Cordes 1986).

It is also important to note that there are a few observations in which the scintillations have such a narrow frequency scale that they can be unresolved in the channel bandwidth of the spectrometer. We apply a simple quadrature correction for the resulting underresolution in frequency. $\Delta\nu_{\rm corr} = \sqrt{\Delta\nu_{\rm iss}^2 - \delta\nu^2}$, where $\delta\nu$ is the channel bandwidth. A similar correction to the timescale $\Delta t_{\rm iss}$ is applied with the 10 s integration time for the spectrometer, in place of the channel bandwidth. There is one case in frequency and one case in time that this correction fails, giving an imaginary estimate; these cases are flagged in tabulating the results with an ellipsis indicating no valid data. There are a few other cases where the scintillations are so slow or so wide in frequency that a single scintle may cover the entire observing range, i.e., $N_{\rm iss} \lesssim 1$, with correspondingly large errors.

[13] With hindsight, the fringe pattern identified by Rickett et al. (1997) can be recognized as a one-sided forward arclet. This can be caused by interference of the unscattered wave with anisotropic scattering from a region that is displaced in the perpendicular direction.

[14] The reciprocal tilt between the asymmetry in the SS and the ACF follows, of course, because they are a Fourier transform pair. Note, however, that the SS is normally displayed with a logarithmic color table—highlighting low power values—whereas a linear color table is usually used for an ACF.

3.2.2. Scintillation Arc Parameters

There is a recognizable scintillation arc structure in more than half of the 54 secondary spectra plots. However, it is difficult to devise a simple yes–no criterion for the presence of parabolic arc structure. Consequently, we have analyzed each observation to estimate a number of specific measurable quantities. We elaborate on this further in Section 5.3, but briefly describe the fundamental quantities here.

We quantify forward arcs in the SS by estimating the curvature η of the underlying parabola $\tau = \eta f_D^2$. We sum S_2 along the parabolas that cover a range in curvature, and in many cases, we find a clear maximum in the summation curve and assign a value η_p to this dominant parabola (Table 3). As already noted, we occasionally also find a bounding arc outside this inner parabola; see Section 5.3 for details.

We also include in the tabulated results a *curvature credibility* criterion, $\eta_{\rm cred}$, for each observation. It is a subjective evaluation of the reliability of the curvature estimate obtained by examining the parabola-summation curve for each case: 2, 1, or 0. A compact maximum in the curve is rated 2; wide and double peaked curves are rated 1; cases where the peak is at the high or low limit in the search range or the SS extends to the Nyquist delay are rated 0. In the latter situation, the DS may be unresolved in frequency, and only an upper limit can be estimated for the decorrelation bandwidth $\Delta\nu_{\rm iss}$. As detailed in Section 5.4, we define and tabulate a width measure $\Delta\eta$ to quantify how sharply S_2 is peaked about the forward parabolic arc.

4. Comments on Individual Sources

Using terminology and results from the previous sections, we qualitatively discuss results from the 22 pulsars below. We group them first by the prominence of the scintillation arc, followed by sorting them in R.A. The three groupings used below have a connection with the $\eta_{\rm cred}$ index. However, the discussion here is on a per-pulsar basis, and a number of pulsars have $\eta_{\rm cred} = 2$ or 1 at one frequency with a lower index at one or more observing frequencies. In some places, the overall signal-to-noise ratio (S/N) will be discussed qualitatively here. We treat it and parameters of the scintillation arcs quantitatively in Section 5.

4.1. Pulsars with a Definite Scintillation Arc

4.1.1. B0450+55 (Figure Set 1.2)

The 1400 MHz observation shows two fairly well-defined scintillation arcs. At 825 MHz, in data taken 14 yr earlier, the scintillation arc structure is not well defined, although there is a hint of an arc coincident with the dashed blue line in the second quadrant of the SS. The CC of the 340 MHz data has a negative power asymmetry (i.e., quadrant (2) power is greater than quadrant (1)), as does the CC at 825 MHz, observed 5 days later. Arc credibility indices $\eta_{\rm cred}$ at 340, 825, 1400 MHz are (0, 1, 1).

4.1.2. B0450–18 (Figure Set 1.3)

We have reported on these observations in detail (Rickett et al. 2021).

However, the 1400 MHz observation was not available at the time of that analysis. In that paper, we found a one-dimensional brightness distribution fit the data well, but the overall brightness function $B(\theta)$ was not consistent with simple Kolmogorov scattering in a thin screen. Instead, $B(\theta)$ scaled with frequency more slowly than Kolmogorov, and various local peaks in $B(\theta)$ were trackable across narrow frequency intervals, but not between 340 and 825 MHz. The 1400 MHz observation was made more than 14 yr after the two at lower frequencies, so the LoS may be probing quite different interstellar medium (ISM) conditions. Two thin scintillation arcs are present. As discussed in Section 5.3.5, neither of these is consistent with the curvature of the *heavily saturated* scintillation arc visible at the two lower frequencies. Hence, this must be due to a different region of scattering along the LoS. Arc credibility indices $\eta_{\rm cred}$ at 340, 825, 1400 MHz are (2, 2, 2).

4.1.3. B0525+21 (Figure Set 1.5)

The 3.7 s pulsar period and nulling causes modulation of the DS in time, particularly with our integration time of 10 s. But a crisscross pattern is clear across the scintles, seen as reverse arclets in the SS. As commented on in Section 5.7, and widely in the scintillation arc literature since Walker et al. (2004), such reverse arclets are indicative of a nearly one-dimensional brightness distribution. Our parabolic summing algorithm (lower right panel) reports a significantly wider arc on the rhs (positive Doppler) than that on the left-hand side (lhs). This is due to the influence of power near the origin; an algorithm that intercepted the apexes of the inverted arclets would produce more nearly equal values of η for the two signs of Doppler frequency. Arc credibility index $\eta_{\rm cred}$ at 1390 MHz is (1).

4.1.4. B0628–28 (Figure Set 1.8)

See Figure 1. These are high S/N observations at all three frequencies. The low-frequency data show a CC core with a clear bounding parabola for power farther from the core of the SS. The 825 MHz observation shows a compact CC core and two scintillation arcs or, alternatively, a boundary arc with an interior arc due to anisotropic scattering and a velocity vector with significant tilt to the major axis of the scattered image (Reardon et al. 2020). The 1400 MHz data are consistent with the trend, seen elsewhere in this survey and in previously published data, for scintillation arcs to become substantially sharper at higher frequency. Arc credibility indices $\eta_{\rm cred}$ at 340, 825, 1400 MHz are (1, 1, 1).

4.1.5. 1508+55 (Figure Set 1.11)

This pulsar, relatively distant (2.10 kpc) for the survey, has the highest transverse velocity (963 km s^{-1}) in the sample and one of the highest of the entire pulsar population. The low-frequency data show a clear CC core plus a very broad scintillation arc that also exhibits strong local maxima in the $B(\theta)$ distribution. This is even more pronounced at 825 MHz, where the highly unusual, flat-topped arclets are a prominent feature. All three frequencies show the presence of the same arc despite the fact that the pulsar has traveled approximately 2900 au transverse to the LoS during this time. Similar flat arclets were recorded by Marthi et al. (2021). Low curvature arclets could be due to localized scattering near the pulsar (i.e., small value of s) interfering with a core in brightness at small angles of deflection. The scattering geometry is complex for this pulsar, as documented by Bansal et al. (2020), who observed remarkable echoes of the pulse arriving 30 ms after

the main pulse at 50 and 80 MHz that persisted over about 3 yr. Also see Sprenger et al. (2022) who develop a two-screen explanation for the scattering from this pulsar. Arc credibility indices $\eta_{\rm cred}$ at 340, 825, 1400 MHz are (2, 2, 2).

4.1.6. B1540–06 (Figure Set 1.12)

This pulsar is similar to B0450–18 and B1508+55, there is a broad scintillation arc at 340 MHz that nevertheless shows signs of broadened arclet structure, confirmed at 825 MHz. It is consistent with highly anisotropic scattering in a plasma screen, with reverse arclets due to narrow peaks in a one-dimensional scattered brightness profile. Arc credibility indices $\eta_{\rm cred}$ at 340, 825, 1400 MHz are (2, 2, 0).

4.1.7. B2021+51 (Figure Set 1.17)

This is an excellent example of no scintillation arc at the lower frequency, but clear evidence for arcs at higher frequency. As discussed in Section 5.8, if we only had the 340 MHz observation, we would classify this as a pulsar without a scintillation arc. Although the DS at 825 MHz shows about a dozen classical scintles, the SS is remarkable in its sharpness and detail. The 1400 MHz observation, offset by 14 yr, is fully consistent with the 825 MHz observation, showing a boundary arc with a filled interior that is similar to the signature expected for an anisotropic image with the major axis not aligned with the effective velocity vector (Reardon et al. 2020). Arc credibility indices $\eta_{\rm cred}$ at 340, 825, 1400 MHz are (0, 1, 2).

4.1.8. B2045–16 (Figure Set 1.18)

Quite similar to B2021+51, this pulsar shows only a hint of a scintillation arc at 340 MHz, but that arc is fully developed—and has a deep unfilled valley—at 825 and 1400 MHz. Nulling of the pulsar causes vertical stripes in the DS that show up as power along the f_D axis in the SS. Arc credibility indices $\eta_{\rm cred}$ at 340, 825, 1400 MHz are (1, 2, 2).

4.1.9. B2217+47 (Figure Set 1.20)

This pulsar, relatively distant ($D = 2.39$ kpc) for this survey, is fairly heavily scattered. It also has a large transverse velocity. It has been extensively studied for interesting propagation effects along the LoS. Michilli et al. (2018) observed pulse echoes delayed by about 10 ms near 150 MHz. They concluded that the echoes, which varied slowly over five years, were scattered by a dense plasma concentration of 100 $\rm cm^{-3}$. Using LOFAR data, Donner et al. (2019) reported an episode of frequency-dependent DM variation toward this pulsar. Similar to B2021+51 and B2045–16, but even more heavily scattered, the SS at 340 MHz is completely dominated by a CC. This is basically true at 825 MHz, too, although there is a hint of a scintillation arc developing. At 1400 MHz, even though the CC is still the dominant feature in the SS, the parabolic summing algorithm shows clear evidence for a broad symmetric scintillation arc. Arc credibility indices $\eta_{\rm cred}$ at 340, 825, 1400 MHz are (0, 0, 1).

4.1.10. B2310+42 (Figure Set 1.21)

Yet another pulsar with a dominant CC at 340 MHz that displays a clear boundary arc at the two higher frequencies. At 340 MHz, the DS has well-resolved scintles with high S/N. The SS shows broad power centered on the origin, with slight positive asymmetry to larger delay. There is a hint of a boundary arc but no valley. At 825 MHz, the DS has about a dozen well-resolved scintles, with no obvious modulation of them. However, the SS has a clear boundary arc with a shallow valley partly filled by SS power extending along the delay axis. The DS at 1400 MHz has three wide, moderately narrow scintles in it, with no obvious intra-scintle modulation. The resulting SS has an outer bounding arc with an inner arc, neither very distinct. The parabolic summing algorithm traces out the bounding arc on the lhs, but it appears to find a faint interior arc on the rhs. Taken together, these data illustrate the value of observing at multiple frequencies. They are consistent with strong plasma scattering with modest anisotropy (Cordes et al. 2006; Reardon et al. 2020). See Section 7 under B2217+47 on the effect of orientation of the anisotropy axis with the $V_{\rm eff}$ vector. Arc credibility indices $\eta_{\rm cred}$ at 340, 825, 1400 MHz are (1, 1, 1).

4.1.11. B2327–20 (Figure Set 1.22)

This set of observations shows the value of scintillation data even when the S/N is not large. At 340 MHz, the DS has only moderate S/N with wide, tilted scintles crossed with finer modulation. There appears to be some broadband pulse modulation, perhaps nulling, which puts power onto the f_D axis. The SS has a clear narrow arc, predominantly one sided (negative asymmetry) with several loci of higher power along the arc. Although it is hard to tell from the low S/N observation at 825 MHz, the DS shows a loosely organized crisscross pattern. The SS has a sharply defined arc with a deep valley and a slight-negative power asymmetry. As can be seen in the quantitative results for η_p in Section 5, the boundary arc detected at 1400 MHz, observed 14 yr after the low-frequency observations, is not consistent with the curvature of the λ^2 scaled values at lower frequencies. $\eta_{p,1400}$ is approximately 7 times greater than $\eta_{p,825}$, when scaled by λ^2. This places the scattering material as close as 40 pc from the Earth. Arc credibility indices $\eta_{\rm cred}$ at 340, 825, 1400 MHz are (2, 2, 0).

4.2. Pulsars with a Probable Scintillation Arc

4.2.1. 0523+11 (Figure Set 1.4)

This is one of the most heavily scattered pulsars in the SAS. With 4096 frequency channels across only 2 MHz of bandwidth, the frequency resolution is barely adequate to resolve the scintles, and even Arecibo's sensitivity is not quite adequate to display a clear SS. However, with a careful choice of the color table, spanning only 10 dB in power, we are able to see a tilted bar of power (negative asymmetry) extending out to more than 200 μs. At 1450 MHz, the tilted SS shows a wide faint arc (negative asymmetry) with shallow valley. It appears that the CC merges into a broad scintillation arc as opposed to being a simple tilted concentration with quasi-elliptical contours. Arc credibility indices $\eta_{\rm cred}$ at 422, 1450 MHz are (0, 1).

4.2.2. B0540+23 (Figure Set 1.6)

This pulsar has very similar scintillation characteristics compared to B0523+11. They both show narrow scintles at the lower frequency, consistent with strong scattering through the same region of plasma. At the higher frequency, a similar

asymmetrical CC emerges with arc-like properties at higher delay. Since a plasma wedge is one mechanism for an asymmetrical power distribution in arcs, the same sense of asymmetry is, perhaps, a linkage in the source of dominant scattering for these two pulsars. We note that they are relatively close on the sky (12.°7) and that B0523+21 and B0540+23 have DMs of 79.4 and 77.7 pc cm^{-3}, respectively. At a screen location of $s = 0.5$, the angular separation would require a transverse screen extent of approximately 190 pc, however. Despite these similarities, the curvature of their scintillation arcs are significantly different, with the value for B0523+11 placing the scattering material about $\gtrsim$600 pc from Earth and about twice that value for B0540+23 (see details in Section 5 and Table 3). Arc credibility indices $\eta_{\rm cred}$ at 432, 1450 MHz are (0, 1).

4.2.3. B0626+24 (Figure Set 1.7)

Both the 432 MHz observation and that at 1390 MHz display a slightly tilted power distribution. At the higher frequency, there is a hint of a scintillation arc in the parabolic sum parameter. Again, as for B0138+59, longer duration observations are necessary because of the particularly long timescale of the scintles. Arc credibility indices $\eta_{\rm cred}$ at 432, 1390 MHz are (1, 1).

4.2.4. B0809+74 (Figure Set 1.9)

There appears to be a bounding arc in the SS of the 340 MHz observations. Observations at the two higher frequencies were too low in S/N and contaminated with RFI in order to show anything clearly in the respective SS. Arc credibility indices $\eta_{\rm cred}$ at 340, 833, 1400 MHz are (1, 0, 0).

4.2.5. B0818–13 (Figure Set 1.10)

The observations at both 340 and 825 MHz are high S/N, but have inadequate frequency resolution. At 1400 MHz, the frequency and time resolution are adequate, and there is some hint of unorganized wispiness around the CC core. Close inspection of the 825 MHz SS shows a slight bifurcation of the power distribution (along the $f_D = 0$ axis) near the Nyquist frequency in delay. Observations of higher-frequency resolution and longer-time duration would be needed to explore further the possibility of a scintillation arc in this pulsar. Arc credibility indices $\eta_{\rm cred}$ at 340, 825, 1400 MHz are (0, 0, 1).

4.2.6. B1706–16 (Figure Set 1.13)

This is a nulling pulsar, which causes extra power along the f_D axis. This is also a low-velocity pulsar, which causes problems because $\Delta t_{\rm iss}$ is long relative to a typical observation length, particularly at the two higher frequencies. The 825 MHz SS suggests a bounding arc with a slight-negative power asymmetry. As was the case with B2310+42, the η_p value on the left looks more reliable than that on the right because of the more prominent boundary arc on the left. Arc credibility indices $\eta_{\rm cred}$ at 340, 825, 1400 MHz are (0, 1, 0).

4.2.7. B1907+03 (Figure Set 1.16)

This single-frequency Arecibo observation has low S/N in the DS. Hence, it is surprising to find a well-delineated patch of power at the origin that extends outward with parabolic wings. A parabola is found on both negative and positive f_D by the weighted summation algorithm. Arc credibility index $\eta_{\rm cred}$ at 1470 MHz is (1).

4.2.8. J2145–0750 (Figure Set 1.19)

This millisecond pulsar ($P = 16$ ms) is lightly scattered in these observations, which is not surprising given its proximity and high Galactic latitude ($D = 0.61$ kpc and $b = -42°$). The S/N of the observations is not large. At 825 MHz there is a faint but definite scintillation arc. The situation is reminiscent of B2327–20 at 825 MHz. In both cases, low S/N scintles are organized in such a fashion that a scintillation arc emerges in the SS. Arc credibility indices $\eta_{\rm cred}$ at 340, 825 MHz are (0, 1).

4.3. Pulsars with No Scintillation Arc or with Data Unsuitable to Determine

4.3.1. B0138+59 (Figure Set 1.1)

A 1 hour data span is not long enough to detect arcs, if they are present. Data are consistent with the CC distribution in the SS given the time–frequency span of the observation. Substantially longer observations than one hour are needed in order to spread out the distribution from the origin along the f_D axis. Arc credibility indices $\eta_{\rm cred}$ at 340, 825 MHz are (0, 0).

4.3.2. B1821+05 (Figure Set 1.14)

This is a single-frequency Arecibo observation. The scintles are short and narrow in frequency, but there is adequate resolution in both dimensions. The SS is CC with weak power extending upward in what might be a bounding arc. Arc credibility index $\eta_{\rm cred}$ at 432 MHz is (0).

4.3.3. B1857–26 (Figure Set 1.15)

Although only 700 pc away, the LoS to this pulsar ($l = 10.°3$, $b = -13.°5$) is heavily scattered. The extremely narrow and brief scintles at 340 MHz make this DS and SS unusable. At 825 MHz, the scintles are easily visible in the the relatively high S/N DS. (There is a defect in the spectrum near 818 MHz that has only been partially corrected in cleaning the data.) The parabola traced out on the SS, determined by the parabolic summing algorithm, is unlikely to be reliable except as a rough guide for the curvature of a scintillation arc that would need to be explored at higher frequency. Arc credibility indices $\eta_{\rm cred}$ at 340, 825 MHz are (0, 0).

5. Analysis of the Secondary Spectra

We report on detailed analysis of the data in this section. The first two subsections present results of a more classical scintillation analysis, focused on the DS. The remainder of the subsections concentrate on detailed analyses of the SS. Throughout Section 5, we refer to parameters extracted from the data set in a uniform manner and presented in Table 3 for all 54 observations.

5.1. Scintillation Parameter Estimation

The scintillation decorrelation time $\Delta t_{\rm iss}$ and bandwidth $\Delta\nu_{\rm iss}$ were already defined in Section 3.2, as the half widths in time and frequency of the ACF $R(\nu, t)$ of the DS. Here we provide additional information about the way we construct $R(\nu, t)$. For many pulsar observations in the SAS, the contribution of noise to the ACF is unimportant. However, noise is significant

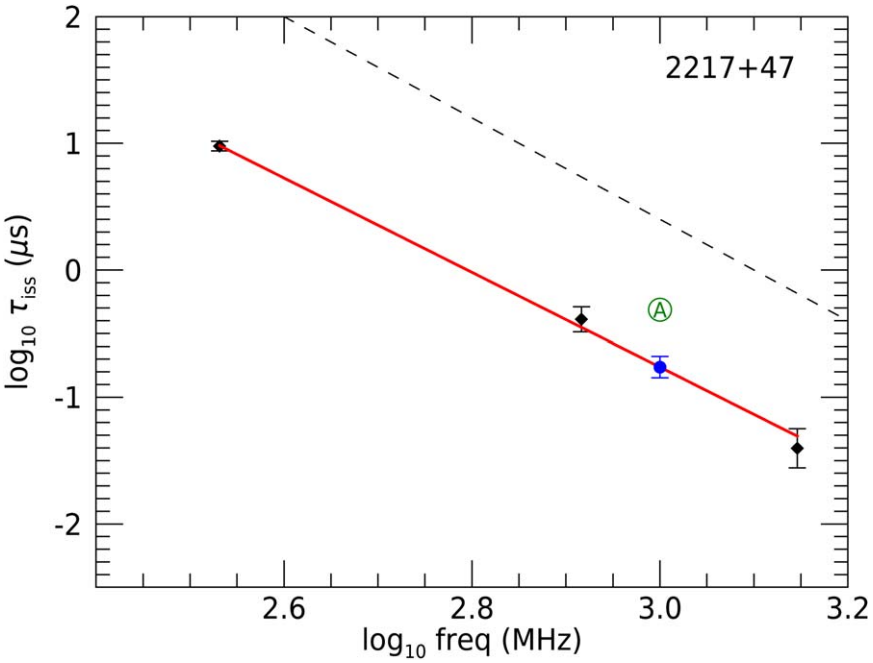

Figure 2. An example of how we calculated $\tau_{\rm scatt,1GHz}$ and its uncertainty for each of the 22 pulsars in the survey. The black points are estimates and 1σ uncertainties of $\tau_{\rm iss}$ at each of the available frequencies. The red line represents the weighted linear least-squares fit through these points. We report a value, marked by a filled blue circle, where that line crosses 1 GHz, and we assign an uncertainty to it from the least-squares fit. The PSRCAT value is marked with a circled green A. The dashed black line has a logarithmic slope of −4. The complete figure set (22 images) is available in the online journal.

(The complete figure set (22 images) is available.)

in some of our data and needs to be corrected. In order to correct the ACF for system noise, we started from S_2 and estimated the mean noise level in the SS from a rectangular region outlined in green in the SS figures away from the ISS. (See Section 5.3 for how we identify a rectangle in delay–Doppler space, where the ISS signal is evident; henceforth, we refer to this as the DD box).

The inverse Fourier transform of S_2, after subtracting the mean noise level from every pixel, yields the ACF of the ISS, $R(\nu, t)$, versus lags in frequency and time. The result, as plotted in the lower left subpanels of Figure 1, is free from a spike at zero lag due to additive white noise, which would be present when the autocorrelation is computed directly from the DS. Hence we use the value $R(0, 0)$ to estimate the scintillation variance, corrected for noise, in defining the decorrelation widths. Its square root gives the rms needed for estimating modulation index.

It also allows us to define S/N as the ratio of the scintillation variance to the noise variance, found by summing the noise level $S_{\rm noise}$ over delay and Doppler. We include this ratio of signal variance to noise variance in Table 3. Note that the S/N for S_2 itself is typically higher, since the ISS only spans part of the observed domain, while the noise is uniform out to the Nyquist points in delay and Doppler. Consequently we also tabulate an S/N for the ISS, defined as the ratio of the variance in ISS summed over the DD box, divided by the variance of the noise, summed over the same DD box, which approximates a matched filter for the ISS. We tested the S/N estimation process against simulated data with known S/N and found it reported accurate values within the statistical uncertainties.

5.2. Pulse Broadening Time

The pulse broadening time $\tau_{\rm scatt}$ is a useful measure of scattering along a LoS and an important parameter to know when planning a timing or scintillation observation. Although many of the parameters in the ATNF PSRCAT database (Manchester et al. 2005) are extremely well determined, others such as $\tau_{\rm scatt,1GHz}$, the pulse broadening time (scaled to 1 GHz), are drawn from a wide range of disparate observational programs conducted over the last 50 yr. The heterogeneous nature of PSRCAT $\tau_{\rm scatt}$ data is increased because values are typically determined by frequency domain techniques for relatively lightly scattered pulsars and time domain techniques for moderate to heavily scattered pulsars. In this section, we report 22 newly determined values of $\tau_{\rm scatt,1GHz}$ and compare them with currently tabulated PSRCAT values.

Figure 2 shows $\tau_{\rm scatt}$ values calculated from the observed $\Delta\nu_{\rm iss}$ values using $\tau_{\rm scatt} = (2\pi\ \Delta\nu_{\rm iss})^{-1}$. The error bars on the individual points are calculated from the formula for the number of independent scintles used by Cordes (1986). Since most of the uncertainties are not too large, we use the approximation of a symmetric uncertainty in the log of the displayed value. The best-fit line represents the weighted ($w_i = 1/\sigma_i^2$) least-squares fit through these points in a log–log representation. The interpolated or, in the case of some pulsars with only two observed frequencies, extrapolated values at 1 GHz are noted with a blue filled circle and a 1σ uncertainty from the linear least-squares fitting process. This is the value and uncertainty reported in Table 4. In the case of a single-frequency observation, $\tau_{\rm iss}$ was determined from the single $\Delta\nu_{\rm iss}$ value assuming $\tau_{\rm iss} \propto \nu^{-4}$.

Figure 3 plots our determinations of $\tau_{\rm scatt,1GHz}$ versus DM. Although the best-fit line has a logarithmic slope close to the value of 2.0 expected for uniformly distributed scattering, we believe that this is coincidental as indicated by the poor match to points with small error bars for data with $\log_{10}$ DM $\gtrsim 1.6$. See further comments below.

Table 4
Scattering Delay and Related Quantities

PSR	Nfreq	$\tau_{\rm scatt,1GHz}$ (ns)	$\delta\tau_{\rm scatt,1GHz}$ (ns)	Slope	δSlope	$\tau_{\rm psrcat}$ (ns)	Ratio $\tau_{\rm psrcat}/\tau_{\rm SAS}$
(1)	(2)	(3)	(4)	(5)	(6)	(7)	(8)
B0138+59	2	60	70	–4.08	0.80	607	9.70
B0450+55	3	33	16	–3.28	0.44	152	4.61
B0450–18	3	380	70	–2.91	0.18	835	2.20
B0523+11	2	4300	110	–3.33	0.03	3036	0.71
B0525+21	1	5000	250	…	…	1518	0.31
B0540+23	2	1900	80	–3.05	0.05	2277	1.20
B0626+24	2	1400	300	–3.36	0.22	8349	6.12
B0628–28	3	40	30	–3	0.60	13	0.30
B0809+74	3	40	40	–2.09	0.98	10	0.24
B0818–13	3	450	70	–3.12	0.15	650	1.44
B1508+55	3	80	20	–3.9	0.25	56	0.74
B1540–06	3	210	40	–3.17	0.21	9	0.04
B1706–16	3	60	20	–3.3	0.37	195	3.10
B1821+05	1	140	16	…	…	5412	37.90
B1857–26	1	800	20	…	…	…	…
B1907+03	1	7800	530	…	…	…	…
B2021+51	3	50	30	–2.82	0.57	197	3.79
B2045–16	3	22	11	–2.85	0.49	5	0.22
J2145–0750	2	40	60	–2.51	1.09	10	0.25
B2217+47	3	170	40	–3.72	0.20	486	2.82
B2310+42	3	90	40	–3.87	0.36	46	0.51
B2327–20	3	21	12	–2.72	0.64	9	0.43

Note. Column (2) is the number of frequencies available to estimate $\tau_{\rm scatt}$. Columns (3) and (4) give the value and uncertainty of $\tau_{\rm scatt}$ that we determine, referenced to $\nu = 1$ GHz using assumed $\tau_{\rm scatt} \propto \nu^{-4}$ relations. See text for details. Columns (5) and (6) give information about the slope of the best-fit line in the equivalent of Figure 4(a) for each pulsar. Column (7) gives the PSRCAT value of $\tau_{\rm scatt}$, also referenced to 1 GHz. Column (8) gives the ratio between the SAS value and the PSRCAT value.

Plots such as this comprised the first observational evidence that showed how the strength of ISS increases with the interstellar column depth of electrons (Rickett 1969). Many studies have shown that $\tau_{\rm scatt}$ typically increases more steeply than $\propto$DM^2 (Sutton 1971; Bhat et al. 2004), expected for uniformly distributed scattering, particularly for longer lines of sight through the Galaxy. Since pulsars are concentrated in the Galactic plane and toward the Galactic Center, the steeper DM dependence is interpreted as increasing concentrations of turbulent plasma toward the inner Galaxy. The survey observations extend only to about 3 kpc and so do not add new distance dependence.

An inspection of individual plots in Figure Set 4 or column (8) in Table 4 shows substantial discrepancies between $\tau_{\rm scatt,1GHz}$ from PSRCAT and those from the SAS. The ratio of the two (column (8)) is evenly split between ratio >1 and ratio <1 (10 instances of each; two comparisons missing). To quantify the severity of the discrepancy, we took all the ratios less than 1 and found their reciprocals. Combining these with the ratios greater than 1, we found the median of the list to be 3.3, giving some indication of the difficulty of measuring this parameter. It is well known (e.g., Gupta et al. 1994; Ramachandran et al. 2006) that $\tau_{\rm scatt}$ is a time variable, sometimes by at least a factor of 3 in both directions, which no doubt accounts for some of the discrepancies in values, both between the SAS values and the PSRCAT values and probably within our own survey.

5.3. Scintillation Arc Curvature

The most fundamental parameter of a scintillation arc is its curvature, η. In this section, we explore many aspects, both theoretical and observational, of arc curvature as it occurs in the survey.

5.3.1. Fundamental Relations

Under the simple hypothesis of partial or fully one-dimensional scattering caused in a single screen located at some distance, the predicted curvature depends on the distances and angles involved as follows (Cordes et al. 2006):

$$\eta = \frac{cD_{\rm eff}}{2\nu^2 V_{\rm eff}^2}, \tag{2}$$

$$\text{where } D_{\rm eff} = D_{\rm psr}(1-s)/s \tag{3}$$

$$V_{\rm eff} = V_{\rm psr}\cos\psi((1-s)/s \tag{4}$$

where the distance of the observer from the pulsar is $D_{\rm psr}$ and from the screen is $(1-s)D_{\rm psr}$; ψ is the angle between the effective velocity $V_{\rm eff}$ and the long axis of the scattering. Alternatively, if the scattering is isotropic, the same relations are obtained with $\cos\psi = 1$. $V_{\rm eff}$ depends on the transverse velocity of the pulsar $V_{\rm psr}$ and also that of the observer and the screen, both of which we assume to be negligible relative to that of the pulsar (see Cordes et al. 2006 for the full expressions).

5.3.2. Methodology for Estimating Arc Curvature

As can be seen in the examples in Figures 1–3, S_2 typically peaks sharply near the origin, and arcs are only recognized at many decibels below the peak. Hence we focus on rectangles in delay and Doppler space away from the origin, selected

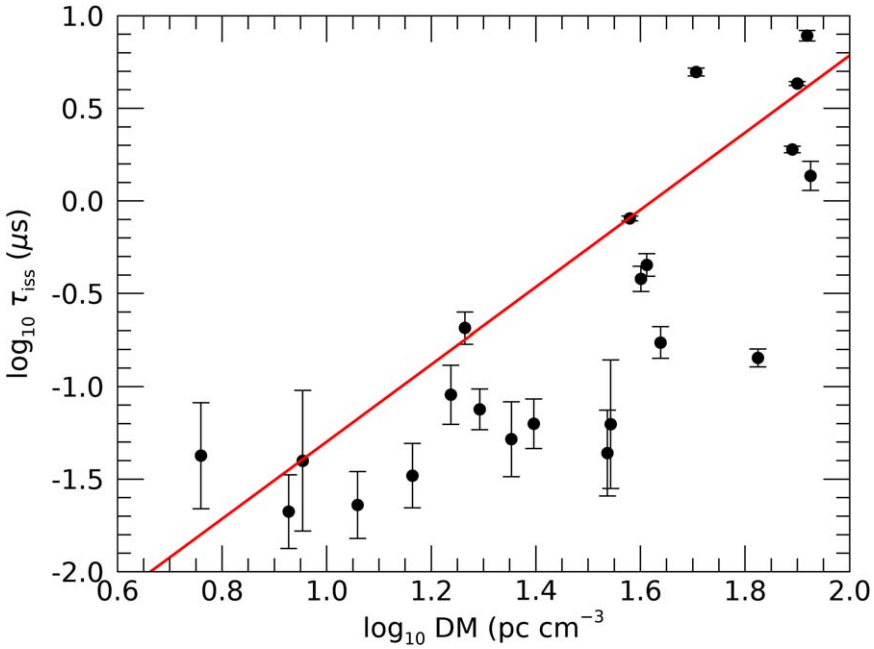

Figure 3. The $\tau_{\rm iss,1GHz}$ values from the SAS are plotted against the DM values. The red line is a weighted least-squares fit. It has a logarithmic slope of 2.08, which is close to the $\tau \propto {\rm DM}^2$ behavior expected for scattering in a uniformly turbulent medium. However, it is clear that the line is a very poor fit to the data if the individual errors are to be believed, and they are well determined at the high DM part of the plot. See the text for further comments.

visually where S_2 is significantly above the noise floor. The rectangles are defined by $f_{DA} > |f_D| > f_{DB}$, $\tau_A > \tau > \tau_B$, which we refer to as the DD box. The curvature is estimated in separate DD boxes for positive and negative f_D, with box coordinates listed in the online version of Table 3.

Elaborating on the discussion in Section 3.2.2, we use two methods to estimate η. In the first, we examine cross-cuts through S_2 over a range of fixed delays. We tabulate the location in f_D of the maximum in each cross-cut separately for both positive and negative f_D. We then fit a parabola to the resulting set of peak locations in (f_D, τ). The fitted curvature is the estimate η_c.

In the second method, we sum S_2 along each parabola from a search range in η_p. Examples of the search, as parabola-summation versus curvature η_p are plotted in the lower right-hand subpanels of Figures 1–3. For each η_p, we compute the sum of $S_2(f_D, \tau) - S_{\rm noise}$ at each delay, interpolated in f_D on each parabola. The search range in η_p is centered on the value $\eta_A = \tau_A / f_{DA}^2$ defined by the parabola that passes through the outer corner of the DD box, with 50 equal steps in log (η) between $0.1\eta_A$ and $10\eta_A$. S_2 is summed in linear power over all delays between τ_B and τ_A and covers f_D out to the Nyquist frequency, but excluding $f_D = 0$. Separate summations over positive and negative f_D are plotted in red and blue, respectively. This method is similar to a Hough transform (Bhat et al. 2016).

The solid lines in Figures 1–3 plot the direct summations, while the lines with "x" markers are summations of S_2 weighted by $|f_D|$. Such a weighting is motivated by the theoretical relationship between S_2 and a one-dimensional model for scattered brightness. In this model (e.g., Stinebring et al. 2019), the S_2 contribution from interference between each pair of brightness components is divided by $|f_D|$, which is thus compensated by the weighting. Note that our weighting is the same as the Jacobian of the transformation to "normalized Doppler profiles" as used in curvature estimation by Reardon et al. (2020), which does not assume one-dimensional scattering. It differs from the theta–theta mapping method of Baker et al. (2022), which is based on one-dimensional scattering.

As a consequence of the weighting, however, an obvious broad peak in the weighted parabola summation, such as in B2217+47 at 340 MHz (Figure 1(c)), does not necessarily correspond to visible parabolic arc structure in S_2. For the same pulsar at 825 MHz, the summation curve only reaches its peak at the maximum curvature searched, and so only a lower limit on η is given. However, the curve does exhibit a sharp rise beyond which it flattens somewhat. This behavior is characteristic of a parabolic boundary in S_2 outside of which S_2 drops off sharply. In the survey, there are several examples of this behavior, which is expected in the presence of a core of lightly scattered waves that interferes with a broadened distribution.

We now compare the two methods of estimating curvature. The estimates of curvature from positive and negative Doppler are averaged for each method giving an overall η_c and η_p for each observation. These are included in Table 3 and compared in the left panel of Figure 4. There is a satisfactory agreement between the two methods. However, since the cross-cut method relies on finding the single highest peak at each delay, it can have quite large errors, and in what follows, we focus on η_p as our curvature estimator. Note that the weighted η_p can give an apparently reliable measure of curvature, even in the absence of a *visible* parabolic arc in S_2. As an example, the SS in the left panel of Figure 1(c) exhibits no arc-like features, but there is a broad peak in the weighted parabola summation defining a specific curvature that is not seen in the unweighted summation.

We include an estimate of the error in curvature, calculated from the upper $\eta_{p,u}$ and lower $\eta_{p,l}$ range for which the parabola summation is above 95% of its peak. This is illustrated in the lower right panels of Figure 1(c). Note, however, that it is not a formal error estimate as we do not have a statistical model for

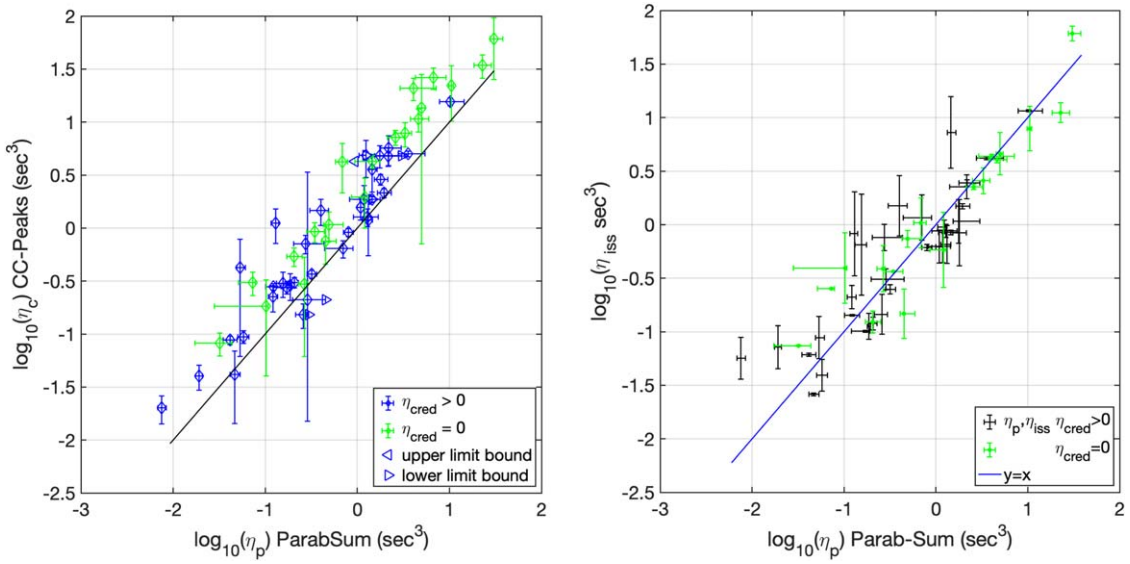

Figure 4. Curvature. *Left*: comparison of the two methods (maxima in cross cuts and parabolic summation) for estimating curvature described in the text, averaged from positive and negative Doppler frequencies. As discussed in Section 3.2.2, we have created a subjective credibility index (0, 1, 2) for the η_p estimate and plot green error bars to indicate low credibility index. *Right*: the pseudo-curvature $\eta_{\rm iss}$, which is defined below in Equation (7), plotted vs. the observed η_p for data with credibility index greater than zero and valid results for the corrected $\Delta\nu_{\rm iss}$ and $\Delta t_{\rm iss}$.

the systematic variations in S_2. We arbitrarily choose 95% reduction since the arcs represent only a small fraction of the total power in S_2 (equal to the variance in the DS), and so also only a small fraction of the parabolic sum. Another estimate could be made at say 50%, which would include a much wider range especially with double peaks and curves that saturate at the search limit. The limits are included with each estimated η_p in Table 3. These limits are also useful in characterizing the width of the arc as elaborated on in Section 5.4.

5.3.3. How Curvature Is Related to the Basic ISS Parameters

Under the same single screen anisotropic scattering assumptions made in Section 5.3.1, we examine the relationship to be expected between the curvature and the basic ISS parameters. The characteristic time and frequency scales are related to the characteristic angular width on the long axis of the scattered brightness at the observer (θ_d) as follows:

$$\Delta\nu_{\rm iss} = c/(\pi D_{\rm eff}\theta_d^2); \tag{5}$$

$$\Delta t_{\rm iss} = c/(2\pi\nu\theta_d\cos\psi V_{\rm eff}). \tag{6}$$

We eliminate the dependence on θ_d in the following combination and obtain a quantity proportional to the curvature in Equation (2).

$$\eta_{\rm iss} = 2\pi\Delta t_{\rm iss}^2/\Delta\nu_{\rm iss} = cD_{\rm eff}/(2\nu^2 V_{\rm eff}^2) = \eta. \tag{7}$$

In the right panel of Figure 4, we plot $\eta_{\rm iss}$ as defined in Equation (7), against the curvature estimated from the parabola summation η_p. The points follow this relation and so confirm our basic assumptions.[15]

Note that this result was already implied in the analysis of arcs by Cordes et al. (2006). They introduced scaled variables p and q as

$$p = 2\pi\Delta\nu_{\rm iss}\tau; \quad q = 2\pi\Delta t_{\rm iss} f_D, \tag{8}$$

which are related by the basic arc equation $p = q^2$. In Section 5.7, we explore what additional insights are obtained from presenting SS in normalized (pq) coordinates.

In the next section, we examine how to use the curvature $\eta_{\rm p}$ or $\eta_{\rm iss}$ to estimate screen distance. However, we note that they both suffer from the same problem: the screen location s and the angle ψ, which appear in $D_{\rm eff}$ and $V_{\rm eff}$, are not separable in a single observation. While there are cases where the orbital motion of the Earth or of a pulsar in a binary system can be used to break this degeneracy (e.g., Stinebring et al. 2005; Reardon et al. 2020; McKee et al. 2022), we do not have a sequence of observations necessary to pursue this further.

5.3.4. Single Screen Model—Estimating Screen Distance

How consistent is the assumption of a single screen (or, more generally, a single *dominant* screen) with the results of the survey? We start from the definition of the theoretical curvature for a mid-placed screen:

$$\eta_{0.5} \equiv \frac{c\,D_{\rm psr}}{2\,\nu^2\,V_{\rm psr}^2} = (0.462\ {\rm s}^3)\frac{D_{\rm psr,kpc}}{\nu_{\rm GHz}^2\,V_{\rm psr,100}^2}, \tag{9}$$

where the pulsar velocity and distance and the observing frequency are expressed in convenient units ($V_{\rm psr,100} = V_{\rm psr}/10^5\ {\rm m\,s^{-1}}$). We can then write Equation (2) as

$$\eta = \eta_{0.5}\frac{s}{\cos^2\psi\,(1-s)}. \tag{10}$$

The theoretical quantity $\eta_{0.5}$ can be evaluated for each observation, using the published values for the pulsar distance and velocity, obtained from PSRCAT and listed in Table 1, for 20 of the 22 pulsars. The left panel of Figure 5 shows the measured curvature (average of η_p from positive and negative f_D) plotted against $\eta_{0.5}$. In the plot, a solid blue line joins

[15] It should be noted that our method of estimating η_p involves visual selection of a rectangle in delay and Doppler, which might contribute to such a trend, because the search range for curvature is based on the apparent width of S_2 in delay and Doppler, which will be inverse-correlated with $\Delta\nu_{\rm iss}$ and $\Delta t_{\rm iss}$, respectively.

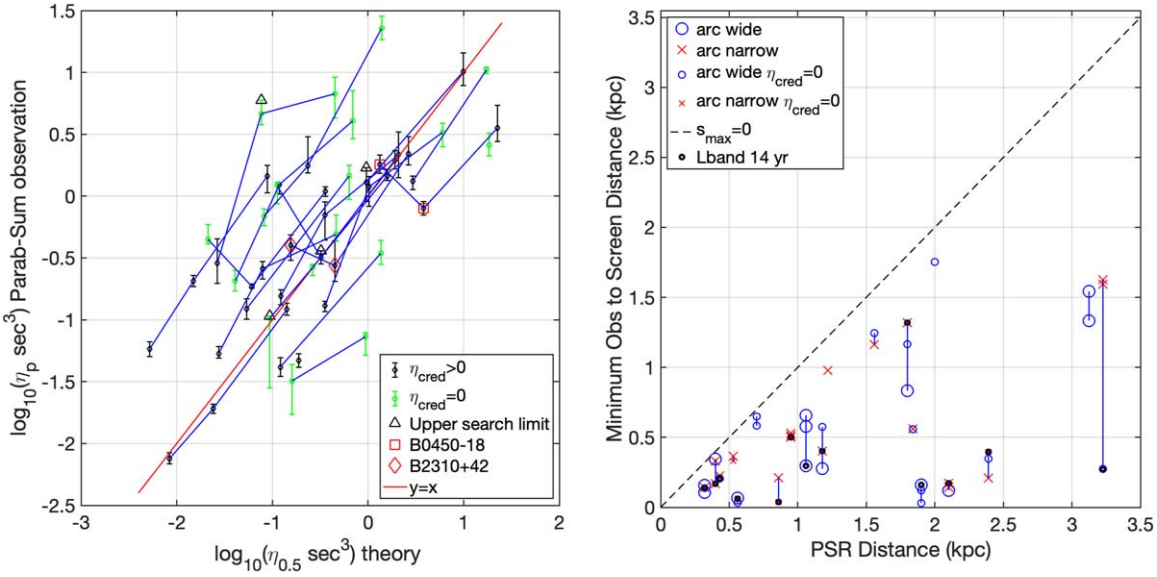

Figure 5. *Left*: curvature η_p vs. single screen theory $\eta_{0.5}$; points without error bars represent estimates with zero credibility index. Points connected by a blue line are from the same pulsar at 2 or 3 frequencies. Two pulsars with discrepant frequency scaling between 1400 and 825 MHz are highlighted. *Right*: single screen hypothesis is distance to the screen ($D_{\rm psr}(1 - s_{\rm max})$) vs. distance to each pulsar, assuming isotropic scattering. If the scattering were anisotropic, this becomes a minimum screen distance. Observations of the same pulsar are joined by a blue line, and marked by a black circle for 1400 MHz observations in 2020. The small symbols mark curvature estimates classified as low credibility. Narrow arcs are defined by $\Delta \log \eta < 0.2$ as estimated from the parabola-summation plots.

observations of the same pulsar at 2 or 3 frequencies. If the values were consistent with each other, the line should have a unit slope (parallel to the red line), corresponding to λ^2 scaling for η. While many show reasonable agreement, there are several discrepancies. There are two pulsars in particular that stand out, B0450–18 and B2310+42, which are highlighted. They are notable because η is larger at 1400 MHz than that at 825 MHz, and so we examine them in detail in Section 5.3.5.

As can be seen in the figure and from Equation (10), the actual value of η can be above or below $\eta_{0.5}$, depending on the values for s and ψ. However, since $\cos^2\psi \leqslant 1$, we can constrain

$$s \leqslant s_{\rm max} = \eta/(\eta + \eta_{0.5}). \tag{11}$$

(This is the same estimate for s used in Putney & Stinebring 2006.)

For isotropic scattering in a single thin screen, the equality can yield a direct estimate of screen distance $D_{\rm scr} = D_{\rm psr}(1 - s_{\rm max})$. In the right panel of Figure 5, we plot such estimates against the distance to each pulsar. Assuming an isotropic single screen scattering model, the 1–3 frequencies observed would yield the same $D_{\rm scr}$; in many cases, the points, joined by a vertical line, do form a cluster. We might expect that low *DM* pulsars can be better modeled by discrete screens causing single or multiple well-defined arcs. Hence we flag the narrow arcs by a red cross, but they show only a weak preponderance for small $D_{\rm psr}$. Another consideration here is the range in observing dates and the substantial proper motion of the pulsars. In particular, the Green Bank observations at 1400 MHz were 14 yr later than the observations at lower frequencies, and are flagged separately.

5.3.5. Apparently Discrepant Frequency Scaling of the Curvature

As noted above, B0450–18 and B2310+42 both show discrepant frequency scaling in the estimated curvature η_p. Figure 1(b) displays the observations for B2310+42 at three frequencies. In each case, the curvature estimation comes from the lower right panel. The major discrepancy is that η_p is a factor 2.5 higher at 1400 MHz than at 825 MHz, but it should be a factor 0.35 smaller. While the observing dates at 340 and 825 MHz differ by only 5 days, the 1400 MHz observations were 14.3 yr later. Similarly for B0450–18, the 1400 MHz observations were 14.4 yr later than those at the lower frequencies. Pulsar B0450–18 moved a transverse distance of 79 au, and B2310+42 moved 376 au in the 14 yr. Many previous arc observations have shown evidence for significant structure in the interstellar plasma on astronomical unit scales, implying that interstellar scattering is due to a very patchy distribution of plasma. Thus we interpret the discrepancies in the frequency scaling as due to changes in the plasma columns over the 14 yr.

These changes in η_p imply localized plasma concentrations at differing distances (unless the scattering were highly anisotropic with a change in orientation to the pulsar velocity), which is also illustrated by the widely differing values of $s_{\rm max}$ in the right-hand panel. For B2310+42 the 825 MHz result shows a well-defined boundary arc whose curvature is 0.2 s^3; scaling this to 1400 MHz predicts 0.07 s^3. However, the value estimated is about 0.3 s^3, but with substantial differences between positive and negative f_D. The SS at 1400 MHz has a poorly defined boundary arc at positive f_D. In a close inspection of the parabolic summation curve, one can see this as a sharp rise in the summation at $\log_{10}\eta_p \sim -1.1$ ($\eta_p \sim 0.08$ s^3), and so might be due to scattering at the same distance as the boundary arc at 825 MHz seen 14 yr earlier.

Now consider the results for B0450–18 shown in Figure 1.3 (and already published by Rickett et al. 2021). At 825 MHz, the strong forward arc has $\eta_p \sim 0.7 \pm 0.3$ s^3 and is modulated by prominent reverse arclets. However, at 1400 MHz, there is a narrow forward arc with curvature $\eta_p \sim 1.8$ s^3, in stark disagreement with the expected scaling from 825 MHz $\eta_p = 0.24$ s^3. Note that in the right panel $s_{\rm max} \sim 0.05$ estimated from the earlier observations of the pulsar at 340 and 825 MHz

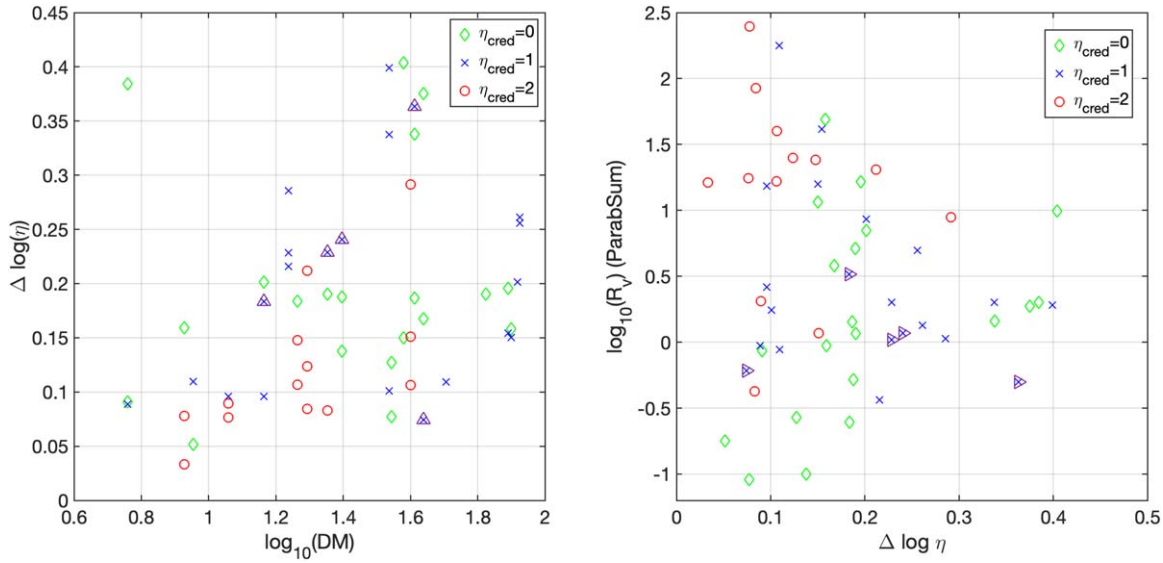

Figure 6. *Left*: arc width vs. DM, flagged by curvature credibility index. *Right*: the depth of the valley in the SS, as a ratio R_v, defined by parabola summation at the estimated curvature divided by a summation of SS near the delay axis. In both left and right panels, points are flagged by the curvature credibility index.

implies a screen near the pulsar. Even though our earlier analysis found anisotropic scattering, a low value of s still holds since $\cos^2\psi \leqslant 1$. Thus the later value of $s_{\max} \sim 0.2$ must be due to a new scattering screen substantially farther from the pulsar.

5.4. Arc Width

We now characterize the relative prominence of arcs in the SS. In particular, we attempt to parameterize the sharpness of an arc by its width and the depth of the valley along the delay axis. Using the analysis from Section 5.3.2, we define a relative width of the arc:

$$\Delta\eta = \log_{10}[\eta_{p,u}/\eta_{p,l}]. \tag{12}$$

The left panel of Figure 6 plots $\Delta\eta$ against DM and shows that arcs at low DM are typically narrow, and at larger DM, the arcs usually widen, and $\Delta\eta$ covers a wide range.

We also use the parabola-summation curves in an attempt to quantify the relative depth of any valley in SS near the delay axis. We divide the peak in the summation curve by the summation of SS parallel to the delay axis (at $f_D = 1$ resolution increment in f_D) over the same range in delay as used in the parabola summation; the result is a ratio R_v between typical SS amplitude along an arc and its value near the delay axis. We avoid $f_D = 0$, which is influenced by the bandpass normalization.

In the right panel of Figure 6, we investigate how R_v is related to the arc width $\Delta\eta$, defined by Equation (12). In the plot, we flag the points by their credibility index. It illustrates how the narrow arcs with deep valleys are often classified as $\eta_{\rm cred} = 2$. Note that in some cases $R_v < 1$, which signifies a ridge along the delay axis rather than a valley, disrupting the curvature estimation. The right panel of Figure 6 shows that narrower arcs are associated with deeper valleys; thus the general increase in $\Delta\eta$ with DM corresponds to a decrease in valley depth R_v with DM. Figure 6 provides observational evidence that narrow arcs with deeper valleys are mostly seen at low dispersion measure. Such a trend is expected since narrow arcs imply localized scattering from a thin region, and at larger distances (or DMs), it becomes more likely that the pulsar signal is scattered in multiple regions making arcs broader and less distinct.

5.5. Theoretical Conditions for Arcs

In Section 5.3.1, we gave the theoretical relations for the curvature of parabolic arcs due to a single localized scattering screen. Here we describe the form of the SS for scattering by random irregularities in electron density, under some specific statistical assumptions, concerning their underlying spatial spectrum and their distribution along each LoS. Consider, first, a thin region modeled as a phase screen at a particular distance along the path from a pulsar. Further, assume transverse variations in the phase that follows the Kolmogorov spatial spectrum.

The ISS observed in pulsars has narrow bandwidth, characterized by $\delta\nu_{\rm iss}$, which is typically much less than the central frequency in the observations. Thus the scintillations are strong in the sense that the rms variation of flux density is comparable to the mean flux density (see, e.g., Rickett 1990). Under strong scintillations, there is negligible flux density from unscattered waves. However, the refractive index in the plasma varies as frequency^{-2}, and at frequencies above about 10 GHz, typically the ISS becomes weak (rms less than mean), and $\delta\nu_{\rm iss}$ increases becoming comparable to the central frequency. Such conditions give rise to a narrow forward arc in the SS caused by the interference of the unscattered wave with an angular spectrum of scattered waves. This forward parabola acts as an outer boundary, below which the SS is zero and above which S_2 is related by a simple expression to the angular spectrum in brightness. At the other extreme, asymptotically strong scattering is due to the mutual interference between all possible pairs of scattered waves, as in the double integral Equation (14) of Cordes et al. (2006).

In Figure 7, we show the SS predicted in asymptotic strong scattering for a screen with a Kolmogorov phase spectrum. The scattering is isotropic in the left panel; it is slightly anisotropic in the center and right panels, with axial ratio $AR = 1.5$ and orientation angles $\psi = 0°$, $90°$, respectively. The SS is

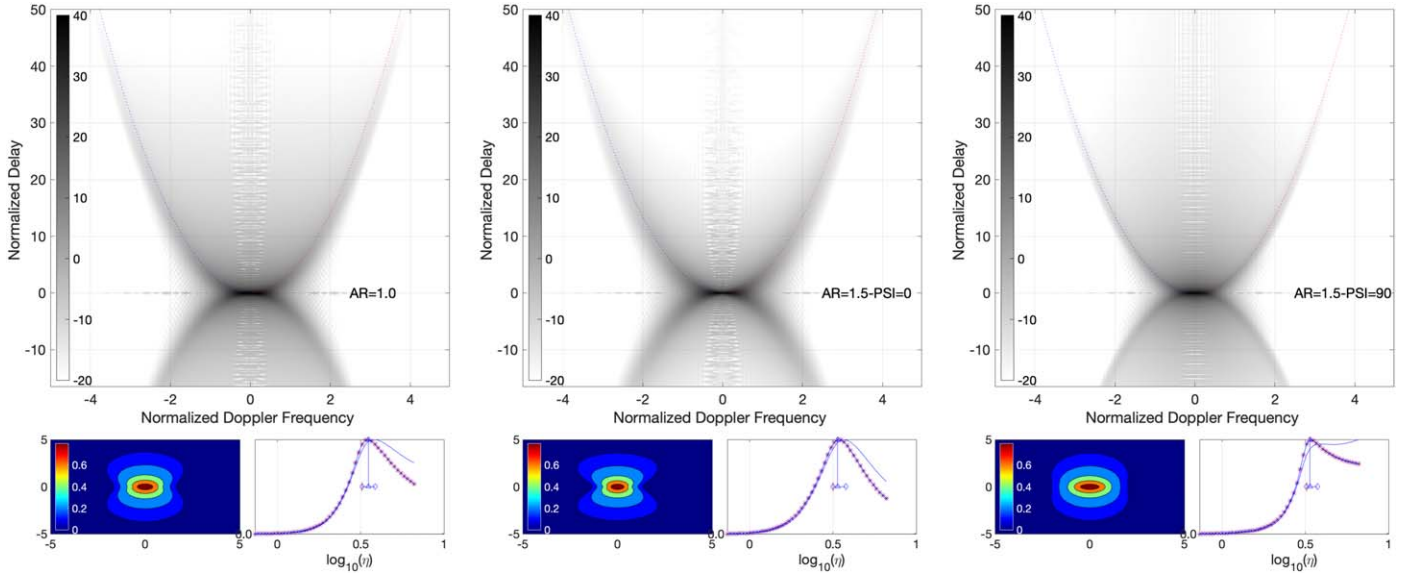

Figure 7. Theoretical secondary spectra for strong scattering in a screen with a Kolmogorov phase spectrum. Format as for the observations. *Left*: isotropic (axial ratio = 1). *Center*: anisotropy axial ratio = 1.5, velocity along major spatial axis ($\psi = 0$). *Right*: axial ratio = 1.5, velocity perpendicular to major spatial axis ($\psi = 90$). The lower left panel is the autocorrelation function $R(\nu, t)$ vs. normalized frequency lag (vertical) and normalized spatial lag (horizontal); the lower right panel is an estimation of parabolic curvature from the secondary spectrum.

calculated numerically by Fourier transforming the expressions for the frequency–time correlation function given by Lambert & Rickett (1999). (Note that the low-level ripples in the SS near the delay axis are due to insufficient dynamic range in the computation.) See Figure 9 and 10 in Reardon et al. (2020) for similar computations, which also exhibit boundary arcs in the secondary spectra.

In all three panels of Figure 7, the parabola-summation curves show significant peaks and yield estimates for both the curvature and the arc width parameter $\Delta\eta$. All three SS plots also exhibit a boundary arc, and demonstrate that boundary arcs do not require anisotropic scattering. They can be seen even with modest anisotropy (axial ratio $AR = 1.5$) and when the orientation angle $\psi = 90°$. The boundary arc is caused by the interference of slightly scattered waves at very small angles with waves scattered at relatively large angles, similar to weak scintillation. It is a property of the isotropic Kolmogorov spectrum that there is a bright compact core in the angular spectrum and also a tail of brightness at larger angles falling as angle$^{-11/3}$. The power-law nature of this tail causes S_2 to decay slowly with delay, making the arc visible out to delays that are many times larger than the characteristic scatter-broadening time.

The center panel ($\psi = 0$, $AR = 1.5$) has the lowest interior SS levels (deepest valley), and the right-hand panel ($\psi = 90$, $AR = 1.5$) has the highest interior SS levels. These differences can also seen from the parabola-summation curves where the peak summation is greater than the summation at the maximum η, where the parabola lies close to the delay axis.

We do not have a full theory for the form of the SS when the scattering is distributed all along the path from the pulsar. Under such conditions, the tight quadratic connection between delay and Doppler frequency breaks down, which will certainly broaden any arcs and broaden any sharp boundary. As a first approximation, the SS can be considered as the superposition of the SS from multiple discrete screens, ignoring the effect of second (or higher) order scattering. This approximation superimposes the parabolic arcs of differing curvatures arising at differing distances and of differing velocities, and any anisotropy would likely be randomized in angle. Thus the overall SS would exhibit few distinct parabolic arcs, but more likely would become quite fuzzy with broadened curves of parabola summation with increased $\Delta\eta$. Note, however, Simard et al. (2019a) describe a precise theory for SS scattered by two discrete screens.

5.6. Arc Width versus Frequency

As discussed throughout Section 4, a striking aspect of the observed SS is the systematic broadening of the arcs at the lower frequencies as in Figures 1(a) and (b), for example. We interpret this as the widening of the scattered brightness distribution as the scintillations become stronger. Here we discuss how the width of the arcs changes for plasma scattering in a single screen with a Kolmogorov spectrum, for which we have a complete theory.

As noted above, a boundary arc is caused by the interference of a bright core of slightly scattered waves with those scattered at relatively large angles, which fall off in brightness as an inverse power law in the Kolmogorov spectrum. The power law is important in that the steeper decrease of a Gaussian spectrum suppresses the amplitude of the arc (see Figures 5 and 7 of Cordes et al. 2006).

Consider now the scaling versus frequency of the SS for an isotropic Kolmogorov spectrum displayed in the left panel of Figure 7. The key idea is that the angular width of the core in scattered brightness increases steeply with wavelength, and so the boundary arc also widens with wavelength.

As noted in Section 5.3.3, the SS from a thin plasma screen can be expressed as a function of normalized delay p and normalized Doppler q. Hence, we can use p, q variables to describe how arcs depend on the observing frequency. Let the delay and Doppler at wavelength λ_1 be τ_1 and f_{D1}. Using p, q from Equation (8), we can scale them to the delay and Doppler

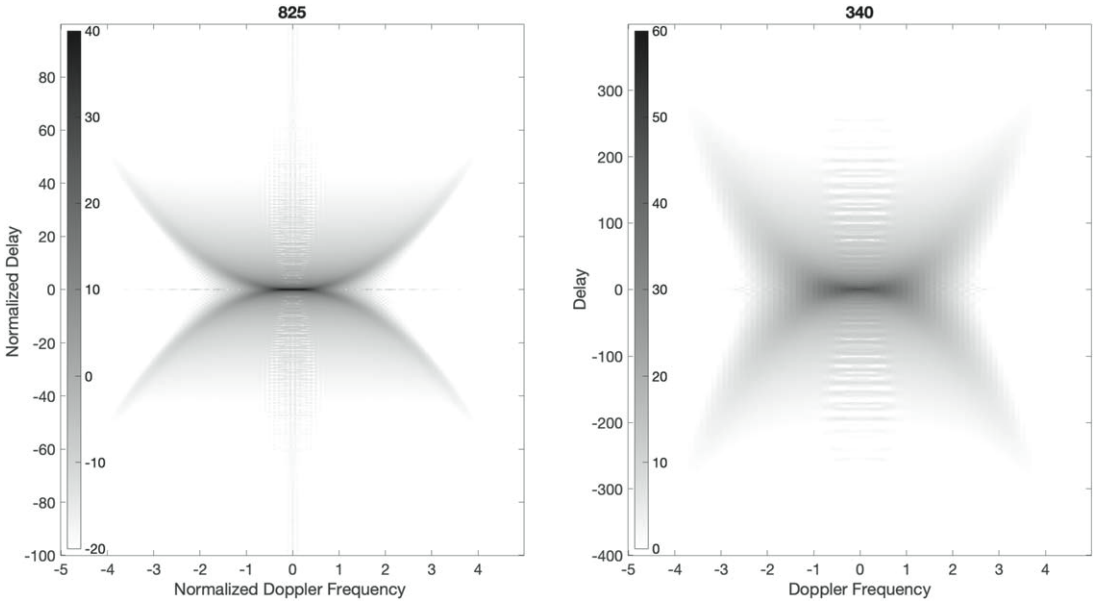

Figure 8. Theoretical secondary spectra for strong scattering in a screen with an isotropic Kolmogorov phase spectrum. *Left*: normalized variables set at 825 MHz. *Right*: stretched to 340 MHz; times $825/340 = 2.4$ in Doppler; and times $(825/340)^4 = 35$ in delay. They are displayed over equal ranges in Doppler and 4 times larger in delay; dynamic range in gray scale is set to 60 dB in both.

at wavelength λ_2 as follows:

$$\tau_2 = p\ D_{\rm eff}\,\theta_{o,2}^2/2c \tag{13}$$

$$= \tau_1\ (\theta_{o,2}/\theta_{o,1})^2; \tag{14}$$

$$f_{D2} = q\ (V_{\rm eff}\,\theta_{o,2}/\lambda_2)$$
$$= f_{D1}\ (\theta_{o,2}/\theta_{o,1})\ (\lambda_1/\lambda_2).$$

$\theta_{o,1}$ is the characteristic width of the scattered brightness function at wavelength λ_1, similarly for wavelength λ_2. For scattering in a plasma, $\theta_o \propto \lambda^2$. Consequently in scaling the calculated SS from a frequency ν_1 to a lower frequency ν_2, the delay axis is stretched by a factor $(\nu_1/\nu_2)^4$, and the Doppler axis is stretched by the lesser factor (ν_1/ν_2). In Figure 8, an example is plotted in which the left and right panels represent 825 and 340 MHz, respectively. The 825 panel is isotropic Kolmogorov calculation from the left panel of Figure 7. The 340 panel is stretched 35 times in delay and 2.4 times in Doppler. Thus the 340 panel is an unequal zoom of the core of the 825 panel, adjusted to the same dynamic range. (If the Kolmogorov scaling exponents were used, the stretch factors would be somewhat larger, 49 and 2.9, in delay and Doppler, respectively). In practical observations, the spectrometer channel width at 340 MHz is much finer than that at 825 MHz, displaying the SS out to much greater delays, which is chosen here to be 4 times greater.

5.7. Analysis of SS Using Normalized (pq) Coordinates

The strong correlation between $\eta_{\rm iss}$ and $\eta_{\rm p}$, described in Section 5.3.3, suggests that we explore the SS in terms of normalized (pq) coordinates, in which a scintillation arc has the simple form $p = q^2$. For convenience, we will call such parabolas pq arcs. In Figure 9, we plot three examples of SS overlaid in pq coordinates, since there is good agreement between $\eta_{\rm p}$ and $\eta_{\rm iss}$.

In panel (a), we have a case of strong inverted arclets and a deep valley along the τ axis, conditions indicative of a nearly one-dimensional scattering profile made up of discrete local brightness peaks (Rickett et al. 2021). It is simple in this case to fit the $\eta_{\rm p}$ parabola since it should coincide with the apexes of the inverted parabolas. However, it is remarkable that the $\eta_{\rm iss}$ parabola has nearly the same curvature since it is determined solely by the widths of the DS ACF—which are (inversely) related to the widths near the origin of the SS—where there is little diffuse power.

Considering Figure 9(b), the power distribution is much more diffuse. Again, the $\eta_{\rm p}$ parabola is determined by the outlying features of the SS, although the precision of its curvature will be hampered by the blurriness of these features. However, the $\eta_{\rm iss}$ parabola, which is just determined by the central region of the DS ACF, matches the $\eta_{\rm p}$ curvature well. Note the wide valley near the τ axis, indicative of anisotropic scattering in a thin screen. This high-velocity pulsar exhibits several intriguing scintillation phenomena that are under current investigation (Sprenger et al. 2022).

Finally, in Figure 9(c) (see also Figure 1(b)), we have almost the opposite situation as in panel (a): it is clear how the DS ACF will yield a good measurement of $\eta_{\rm iss}$ because there is power centered on the origin in the SS, but it is surprising that a (weighted by $|f_D|$) parabolic summing of power along the SS plane results in such close agreement with the ACF-determined $\eta_{\rm iss}$ value.

5.8. Scintillation Arcs Tend to Disappear at Low Frequency: Is This a Problem?

The multifrequency aspect of this survey is a key asset, particularly when observations were made within a few days of each other as were the Green Bank 340 and 825 MHz observations and observations of the three Arecibo pulsars with multifrequency data. Consider a direct comparison of the SS for pulsar B2021+51 at 340 and 825 MHz as shown in the left two panels of Figure 10.

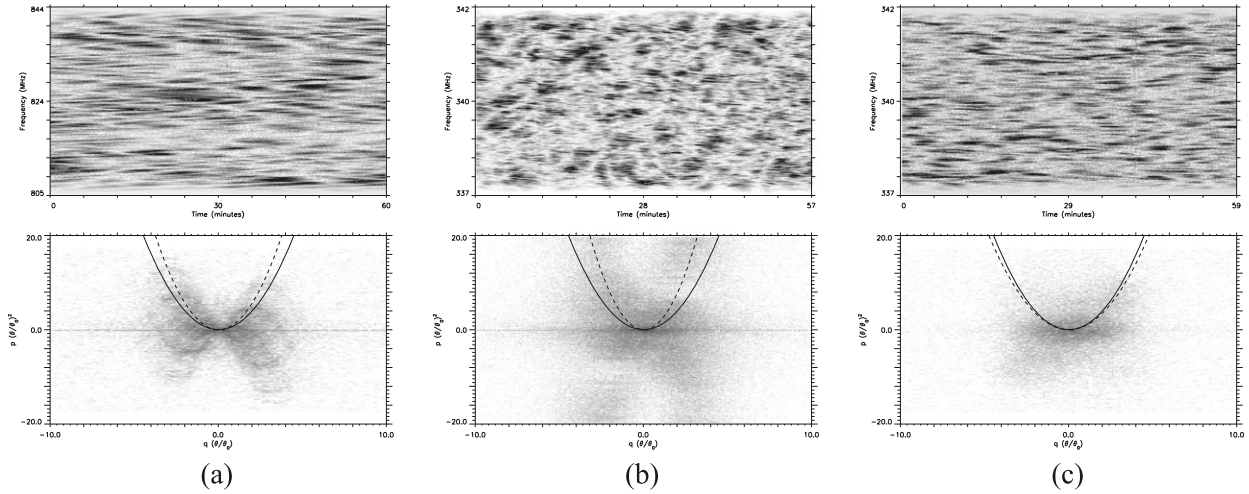

Figure 9. Comparison of arc-based curvature estimate ($\eta_{\rm p}$) with ISS-parameter-based curvature ($\eta_{\rm iss}$) for secondary spectra using normalized (p, q) coordinates. All three panels are plotted to the same limits in p and q and hence can be directly compared. The dashed line follows the $\eta_{\rm p}$ parabola; the solid line indicates the $\eta_{\rm iss}$ parabola. (a) B0450–18 observed at 825 MHz (Figure Set 1.3). (b) B1508+55 observed at 340 MHz (Figure Set 1.11). (c) B2310+42 observed at 340 MHz (Figure 2 and Figure Set 1.21).

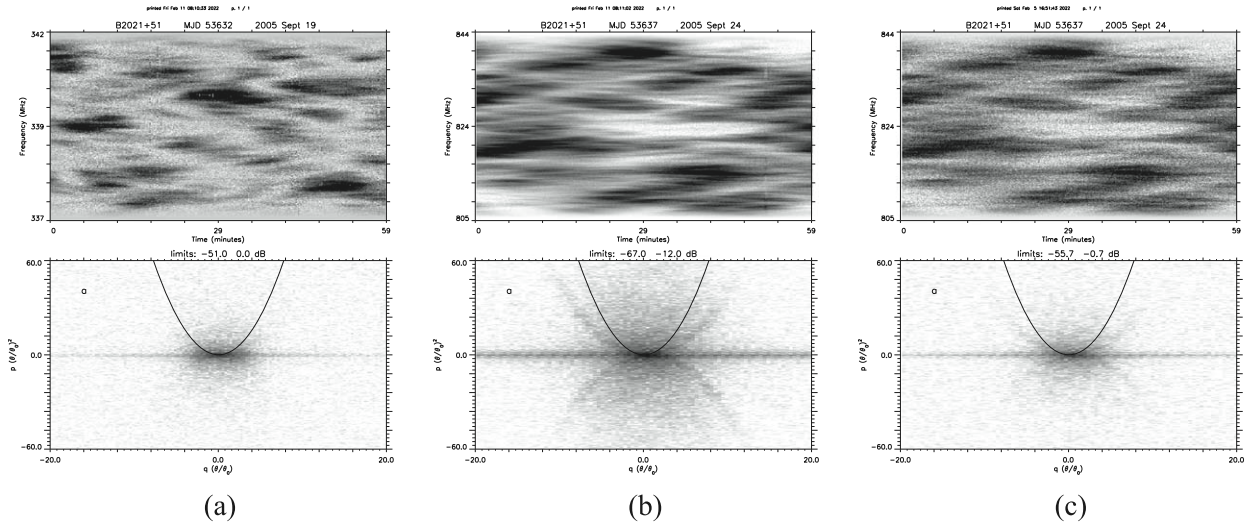

Figure 10. Dual frequency comparison of secondary spectra using normalized (p, q) coordinates. (a) B2021+51 at 340 MHz. Display is a linear gray scale for the DS and logarithmic gray scale for the SS, covering about 50 dB from white to black. A pq arc ($p = q^2$) is superposed on the SS. Since p and q are normalized by the angular width of the corresponding $B(\theta)$ curves, the axis stretch factors are accounted for automatically. (b) B2021+51 at 825 MHz observed 5 days later than that in the left panel. Display style is the same as in panel (a). (c) Same data as in (b), but with Gaussian white noise added to approximately match the S/N ratio of panel (a).

The pq arc does not coincide with the boundary arc. However, this could simply be due to a misestimation of the $\Delta\nu_{\rm iss}$ and $\Delta t_{\rm iss}$ parameters, a more exaggerated form of the case shown in Figure 9(a). The more important difference between panels (a) and (b) is the absence of a boundary arc at the lower frequency. Is this surprising? Displaying the SS using normalized coordinates should remove the issues with scaling of axes that were discussed in Section 5.6. If the underlying assumptions hold, the low-frequency SS should appear similar to that of the high-frequency one in this normalized display.

The main additional assumptions are (reordered to match the list order) as follows: an inhomogeneity spectrum in the screen that supports fluctuations at a small enough spatial scale to provide the high angle scattering needed to produce the arc; thin screen scattering with a screen that does not truncate the beam at lower frequency (Cordes & Lazio 2001; Geyer et al. 2017); and adequate S/N ratio to detect a scintillation arc.

Here we explore these possibilities:

1. *Truncated screen.* The scattered beam has become so large that it extends beyond the physical extent of the scattering material.
2. *Inner scale.* There are no plasma fluctuations present at the small physical size needed to produce the halo power.
3. *S/N inadequate*. The observation at 340 MHz has insufficient sensitivity to reveal the low-level scintillation arcs at high delay.

Considering the first possibility, we use the information in Tables 1 and 3 to find that the screen must deflect a maximal ray at 340 MHz by about 2 mas. The coherence scale s_0 in the screen necessary to do so can be found from $s_0 = \lambda/(2\pi\theta_{\rm scatt})$ (e.g., Equation (2.4) in Rickett 1990) and is $s_0 \approx 1.5 \times 10^4$ km. This is substantially larger than the values of the inner scale of turbulence, which are in the range ∼200–2000 km (Spangler & Gwinn 1990; Molnar et al. 1995; Bhat et al. 2004; Rickett et al. 2009). Hence, it is unlikely that the absence of a scintillation

arc at 340 MHz is caused by a deficit of irregularities at the coherence scale.

Possibility two proceeds similarly. The width of the 340 MHz beam as it passes through the screen is ≈2 au, a typical value for pulsars in this survey. In order for this to explain the absence of a scintillation arc at 340 MHz, there would need to be a gap of this size in the medium producing the scattering. The material that produces the scintillation arc observed five days later at 825 MHz would need to comprise a small areal fraction of the ∼35 times larger low-frequency beam and hence be diluted in its ability to produce a scintillation arc. While not impossible, this seems unlikely.

Finally, we consider the option that the S/N of the 340 MHz observation is insufficient to allow detection of a scintillation arc. As is evident from inspection of the figures and Table 3, the S/N at 340 MHz is substantially lower than that for the 825 MHz observation. When we approximately match the S/N of the two observations by adding white Gaussian noise to the 825 MHz data, we obtain the result in Figure 10(c). Although there is a hint of a scintillation arc visible, slightly more additive noise would suppress the arc at 825 MHz entirely. Hence, we consider this to be the most likely explanation: the observation was simply not sensitive enough to detect the presence of the arc visible in the 825 MHz data.

6. Discussion

We draw a number of conclusions from the qualitative and quantitative analysis of the survey data in the preceding sections. We discuss those conclusions below.

6.1. Scintillation Arcs Are Prevalent

Satisfactory S/N was obtained in 54 observations of 22 pulsars (at 1–3 frequencies) whose DMs range from 5.7 to 84 pc cm^{-3}. Estimates of characteristic widths in frequency $\Delta\nu_{\rm iss}$ and time $\Delta t_{\rm iss}$ were obtained from the ACFs of DS. In all cases, a curvature estimate was made by summing SS along forward parabolas, weighting $\propto |f_D|$. In more than half the observations, the summation exhibits a credible peak from which a curvature η_p was estimated, and a relative width parameter $\Delta\eta$ is defined. These estimates are classified by a subjective credibility index ($\eta_{\rm cred}$: 0, 1, 2). Of the 54 observations, 13 ranked as 2, 21 ranked as 1, and 20 ranked as 0. Thus we have evidence for forward arcs in 34 of 54 observations. In observing 22 pulsars, 19 exhibited an arc ranked $\eta_{\rm cred} \geqslant 1$ at one frequency or more.

6.2. Scintillation Arcs Are More Prominent at Higher Radio Frequencies

As discussed in Section 5.6, the much stronger scaling of the SS delay axis with frequency compared to the scaling of the Doppler axis results in the suppression of scintillation arcs at a radio frequency that depends upon the degree of scattering along the LoS.

6.3. Scintillation Arcs Are Narrower in Low DM Pulsars

Figure 6 demonstrates that narrow well-defined arcs are common at low DM, but become rare at higher DM. It is well established that a sharp scintillation arc can only be produced if the dominant scattering occurs in a relatively small fraction of the LoS, what is commonly referred to as a *thin screen*, although the transverse extent of the scattering region and its physical characteristics are left unspecified, e.g., Walker et al. (2004); Cordes et al. (2006). Many of the narrower arcs at low DM are consistent with scattering from a localized plasma screen whose distance from the pulsar is no more than $s_{\rm max} D_{\rm psr}$.

The trend toward narrow arcs at low DM follows naturally from a model for the ISM in which a pervasive but relatively low-scattering plasma is combined with isolated regions or *clouds* of enhanced electron density $\langle n_e \rangle$, enhanced electron density variance $\langle n_e^2 \rangle$, or both. Such a trend is to be expected if the scattering is distributed along the LoS from each pulsar. This decrease in arc definition with path length could be due to either multiple thin regions along the path or a more general extended distribution in the scattering plasma.

6.4. Narrow Arcs Do Not Imply Anisotropy

Narrow arcs do not, by themselves, imply an anisotropic plasma, but they are consistent with a power-law spatial spectrum. The rich detail revealed in the reverse arclets reported for B0834+06 implies highly anisotropic plasma structures in the local ISM (Hill et al. 2005; Brisken et al. 2010). The main forward arc with a deep valley along the delay axis in B1133+16 is also evidence for highly anisotropic local scattering (Stinebring et al. 2019). However a result of our analysis is the recognition that boundary arcs do not necessarily imply anisotropic scattering (see also Reardon et al. 2020). Under the conditions of strong scintillation that apply to our observations, the relatively narrow boundary arcs can be caused by isotropic scattering when the underlying plasma density fluctuations follow some types of power law versus wavenumber. While we have shown examples from screens that follow the Kolmogorov turbulence spectrum, other power-law spectra can also cause forward arcs. As analyzed earlier by Cordes et al. (2006), forward arcs can be expected from spectra with a range of power-law exponents; the simplest way to characterize them is via the structure function for phase perturbations that they impose on a propagating radio wave. Cordes et al. (2006) show examples with phase structure functions that follow a power law versus spatial lag having exponents $\alpha \leqslant 2$, where the corresponding exponent in a three-dimensional wavenumber spectrum is $\alpha + 2$. The key point is that no extended arcs are seen unless $\alpha < 2$. Media consisting of Gaussian-profiled density concentrations causing interstellar lenses are likely modeled by $\alpha = 2$, and so probably do not manifest parabolic arcs. Thus the defining property of the plasma density structures that causes arcs is the form of their high wavenumber spectrum rather than any anisotropy. Kolmogorov turbulence provides one possible physical origin for such fine scales in the plasma.

6.5. Reverse Arclets and Power Asymmetries Indicate a Patchy Scattering Medium

Reverse arclets are seen in the SAS in the following pulsars (see Section 4 for more details): B0450–18, B0525+21, B1540–06, and B2327–20, whose distances range from 0.4 to 1.2 kpc. In addition, B1508+55 ($D = 2.10$ kpc) shows discrete arclets, which appear to be flat (i.e., low curvature). Overall the presence of arclets, and the relative frequency independence of their inferred angular locations (Hill et al. 2005), implies highly localized centers of scattering (or refraction) across the transverse dimension and an anisotropic

Table 5
Scintillation Arcs: Power Asymmetries and Discrete Structure

PSR	Asymmetry[a]	Discrete Structure	$l_{10\ \mathrm{mHz}}$[b] (au)
(1)	(2)	(3)	(4)
B0450+55	neg (340)		1.0
B0450–18		(825)	11.4
B0523+11	neg (1450)		1.1
B0540+23	neg (430, 1450)		1.8
B0626+24	pos (430)		5.2
B1508+55		(340, 825, 1400)	0.3
B1540–06		(340, 825)	3.2
B2310+42	pos (340)	(825)	2.4
B2327–20		(340)	1.0

Notes.
[a] Numbers in parentheses indicate data set frequency in MHz. Negative (neg) asymmetry means stronger power for positive delay on the negative side of the f_D axis; conversely for positive (pos) asymmetry.
[b] Approximate physical size (astronomical unit, or au) on the screen with these assumptions: $s = 0.5$, $f_D = 10$ mHz, $\nu_0 = 1$ GHz, velocity dominated by the pulsar. Scalings: $l_{10\ \mathrm{mHz}} \propto sf_D/(V\nu)$.

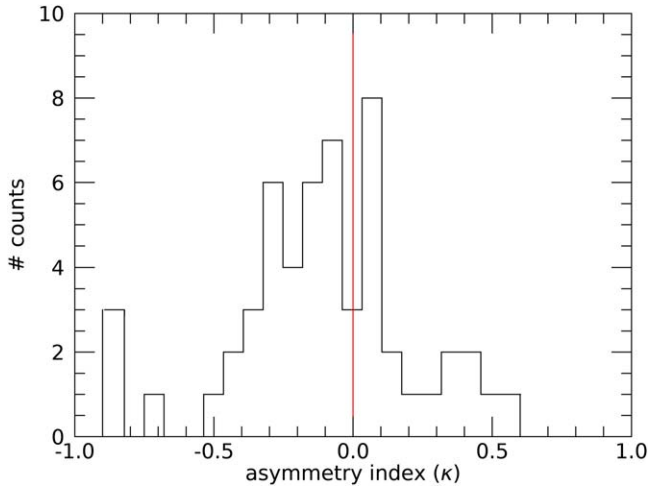

Figure 11. Histogram of arc power asymmetry index defined as $\kappa \equiv (R - L)/(R + L)$, where R is the arc power for $f_D > 0$, and L is the arc power for $f_D < 0$. Negative values of κ represent scattering material out in front of the projected path of the pulsar across the sky.

image on the sky (Walker et al. 2004; Cordes et al. 2006; Pen & Levin 2014; Reardon et al. 2020).

Power asymmetries in the SS along the scintillation arc and, in particular, between negative and positive f_D values, have been noted since early in the study of the phenomenon (Cordes et al. 2006). In addition, discrete patches of power can be present, generally associated with reverse arclets. In a few cases, it has been possible to track their motion from negative to positive f_D values along the arc (Hill et al. 2005; Wang et al. 2018). We see evidence of both phenomena in the survey data. The occurrence of power asymmetry and discrete structure in scintillation arcs for the 22 pulsars in the survey is summarized in Table 5.

Two explanations have been advanced for power asymmetry along the arc: (1) the presence of a refractive gradient across the image (Cordes et al. 2006; Coles et al. 2010; Reardon et al. 2020) and (2) spatial variation of the properties of the scattering screen transverse to the LoS (e.g., Hill et al. 2005). These mechanisms are not mutually exclusive because a patchy medium, by which we mean variations in the scattering strength transverse to the LoS, will necessarily have substantial n_e gradients.

In Table 3, the asymmetry index κ quantifies the power along the lhs (negative f_D; $\kappa < 0$) of the arc compared to along the rhs. In Figure 11, we note a *slight* tendency toward more instances of negative κ values (33 versus 21 positive), and the four largest values of $|\kappa|$ are all negative. However, the sample is small, and this is likely a statistical fluctuation. (The $f_D < 0$ side of the SS is the material that is out in front of the projected path of the pulsar across the sky (Hill et al. 2005).)

Kolmogorov density variations do not, in general, lead to substantial refractive shifts of the image. In particular, it is rare to find refractive shifts as large as the width of the scattering disk size. There is no way to adjust this fact for a Kolmogorov medium because it arises from the relative shallowness of the inhomogeneity power law. During the 1980s, this was a subject of substantial theoretical attention with a leading idea being the inhomogeneity power laws with an index $\beta > 4$, where this index in the inhomogeneity power law has a value of $\beta = 3.67$ for a Kolmogorov medium (Blandford & Narayan 1985; Goodman & Narayan 1985; Romani et al. 1986; Goodman et al. 1987). As an alternative to explanations associated with power-law density variations, the idea of discrete lenses was introduced (Clegg et al. 1998). More recently, highly inclined corrugated sheets viewed at nearly grazing incidence (Pen & King 2012; Pen & Levin 2014) and noodle-like models (Gwinn 2019; Gwinn & Sosenko 2019) have been proposed.

As can be seen in Table 5, just under half of the pulsars in the survey show evidence for power asymmetry or discrete structures in the SS or both. The last column in this table presents an approximate size scale, $l_{10\ \mathrm{mHz}}$, probed by the scintillation arc observations. Note that in the SS it is the separation of features in two coordinates, Doppler and delay, that allows discrete patches of power to be identified. On the other hand, the occurrence of tilted scintles in the DS was noticed soon after the development of systematic scintillation observations (Hewish 1980 and references therein).

The evidence for thin screen regions of scattering implies localization along the LoS direction. Together with the power asymmetries and reverse arclet structure in the SAS, these paint a picture of a very patchy distribution in the plasma responsible for the ISS within the ~3 kpc region sampled.

6.6. The Galactic Distribution of Plasma Scattering

The study by Alves et al. (2020) revealed a coherent sheet-like structure that they refer to as the Radcliffe Wave, a 2.7 kpc long filament of gas corresponding to the densest part of the Local Arm of the Milky Way. In addition, the understanding of the Local Bubble has improved markedly with the recent publication by Zucker et al. (2022). There, using new spatial and dynamical constraints including recent Gaia data and carefully curated velocity information, they produce a three-dimensional map of dense gas and young stars within 200 pc of the Sun. They find evidence for stars preferentially concentrated near the edge of the Bubble at about 100 pc from the Sun. The boundaries are seen to be star-forming regions and are partially ionized by UV radiation from nearby stars. The structure and distribution of truly Local Interstellar Clouds is also relevant. Linsky et al. (2019) and Linsky & Redfield (2021) find partially ionized clouds on the scale of parsecs.

Our survey for scintillation arcs provides evidence for occasional localized plasma concentrations within about 1 kpc (Sections 6.1 and 6.2). The observations are consistent with the earlier, more detailed observations of multiple discrete arcs in some nearby pulsars (e.g., Putney & Stinebring 2006; see also Reardon et al. 2020). The reverse arclet phenomenon gives further evidence for discrete plasma concentrations down to astronomical unit scales. However, the physical origin of the clumps remains a mystery.

The evidence for the isolated concentrations of scattering plasma has to be reconciled with the strong evidence that the interstellar scatter broadening time for pulsars increases steeply with DM, and so with pulsar distance. There is an absence of narrow arcs from pulsars beyond a few kiloparsec in our survey, which is consistent with cumulative scattering along the LoS from many such concentrations at a wide range of distances (and so with differing arc curvature). At present we lack a proper theory for the SS that would be observed through multiple plasma screens. While the SS from nearby pulsars can be understood by the superposition of arcs singly scattered by each screen, the SS due to successive scattering by multiple plasma screens have not been studied beyond the two screen analysis of Simard et al. (2019a).

Pulsar dispersion and scattering studies over more than 40 yr have resulted in a fairly consistent picture of the ionized gas within ∼5 kpc of the Sun (Taylor & Cordes 1993; Cordes & Lazio 2002 [NE2001]; Yao et al. 2017). Overall, the geometry consists of relatively sparse regions of enhanced plasma scattering on scales smaller than 1 kpc that are increasingly concentrated toward the Galactic plane and toward the center of the Galaxy. The models typically assume that the plasma density is *turbulent*, following a power-law spectrum versus wavenumber over the microscales responsible for the ISS, but the strength of the turbulence varies widely over the much-larger Galactic scales. Thus the turbulence level varies on scales ranging from parsecs to astronomical unit and indeed down to the diffractive scale at 10^6–10^8 m. In NE2001 some such concentrations are identified as known H II regions, but other clumps of denser scattering are added to model the specific pulsars that exhibit extra scatter broadening. (See Mall et al. 2022 for an in-depth study of one such region associated with the pulsar J1643–1224 seen behind the H II region Sh 2–27.)

In order to model the arclet phenomenon and the multiple forward arcs in pulsar B1133+16 (see McKee et al. 2022; and Putney & Stinebring 2006, for example), many more clumps are implied. A smaller scale is needed such that the mean free path for a pulsar sightline to intersect a clump is on the order of 100–500 pc. Ocker et al. (2021) have proposed turbulence at stellar bow shocks as the possible location of enhanced scattering. Scattering could even be caused in the plasma spheres that surround hot stars, while Walker et al. (2017) proposed elongated plasma structures drawn out in the stellar winds from hot stars. Motivated by evidence of extreme one-dimensional scattering images for some pulsars, Pen & Levin (2014) proposed weak waves propagating along magnetic domain boundary current sheets as the origin of scintillation arcs.

The foregoing discussion suggests the big-picture hypothesis that the arc-causing clumps are so widely distributed *that they are the building blocks for all of interstellar scattering*. We suggest that the ISM contains multiple bubbles creating a foam-like structure with compressed regions of gas (neutral and plasma) at their interfaces, some of which cause observable arcs. The 50–100 pc distance is comparable to the distance between the arc-causing clumps in the LoS to B1133+16 for which McKee et al. (2022) identified six discrete arc-causing screens along the 360 pc LoS. If this path is typical of much-longer paths through the Galaxy, it would explain the rarity of narrow arcs at higher DM, since it would be unlikely that a single arc would dominate the SS for pulsars beyond a kiloparsec or so. Thus it becomes interesting to determine whether the arc-causing screens have a characteristic radius and scattering measure. Under the Kolmogorov scenario, the radius might be identified with the outer scale of turbulence, as in NE2001.

7. Summary

We summarize our main results as follows:

1. Scintillation arcs are prevalent.
2. Scintillation arcs are more prominent at higher radio frequencies.
3. Scintillation arcs are narrower in low DM pulsars.
4. Narrow arcs, especially sharp boundary arcs, do not imply anisotropy.
5. Reverse arclets with deep valleys are seen in about 20% of the survey pulsars.
6. Power asymmetries in arcs indicate a patchy scattering medium on an astronomical-unit-size scale.

Overall, combining the SAS results with earlier ISS studies suggests that interstellar scattering is largely caused at the boundaries of structures in the plasma density similar to the Local Bubble.

We thank the developers and maintainers of the ATNF pulsar database PSRCAT (Manchester et al. 2005), which we used extensively. M.A.M., S.M.R., and D.R.S acknowledge support from the NSF from a Physics Frontiers Center award (2020265) to NANOGrav. In addition, D.R.S. thanks the NSF for support through grant 2009759. S.M.R. is a CIFAR Fellow. S.K.O. acknowledges support from the National Aeronautics and Space Administration (NASA 80NSSC20K0784). The Green Bank Observatory is a facility of the National Science Foundation operated under cooperative agreement by Associated Universities, Inc. The Arecibo Observatory is a facility of the NSF operated under cooperative agreement (#AST-1744119) by the University of Central Florida in alliance with Universidad Ana G. Mendez and Yang Enterprises, Inc. The National Radio Astronomy Observatory is a facility of the National Science Foundation operated under cooperative agreement by Associated Universities, Inc.

Facilities: GBT, Arecibo.

Objects: PSR B0138+59, PSR B0450+55, PSR B0450-18, PSR B0523+11, PSR B0525+21, PSR B0540+23, PSR B0626+24, PSR B0628-28, PSR B0809+74, PSR B0818-13, PSR B1508+55, PSR B1540-06, PSR B1706-16, PSR B1821+05, PSR B1857-26, PSR B1907+03, PSR B2021+51, PSR B2045-16, PSR J2145-0750, PSR B2217+47, PSR B2310+42, PSR B2327-20.

ORCID iDs

Dan R. Stinebring https://orcid.org/0000-0002-1797-3277
Barney J. Rickett https://orcid.org/0000-0002-1138-2417

Anthony H. Minter https://orcid.org/0000-0002-6555-312X
Alex S. Hill https://orcid.org/0000-0001-7301-5666
Adam P. Jussila https://orcid.org/0000-0002-8380-6688
Lele Mathis https://orcid.org/0000-0003-3491-1024
Maura A. McLaughlin https://orcid.org/0000-0001-7697-7422
Stella Koch Ocker https://orcid.org/0000-0002-4941-5333
Scott M. Ransom https://orcid.org/0000-0001-5799-9714

References

Alves, J., Zucker, C., Goodman, A. A., et al. 2020, Natur, 578, 237
Baker, D., Brisken, W., van Kerkwijk, M. H., et al. 2022, MNRAS, 510, 4573
Bansal, K., Taylor, G. B., Stovall, K., & Dowell, J. 2020, ApJ, 892, 26
Bhat, N. D. R., Cordes, J. M., Camilo, F., Nice, D. J., & Lorimer, D. R. 2004, ApJ, 605, 759
Bhat, N. D. R., Ord, S. M., Tremblay, S. E., McSweeney, S. J., & Tingay, S. J. 2016, ApJ, 818, 86
Blandford, R. D., & Narayan, R. 1985, MNRAS, 213, 591
Brisken, W. F., Macquart, J.-P., Gao, J. J., et al. 2010, ApJ, 708, 232
Chen, J. L., Wen, Z. G., Yuan, J. P., et al. 2022, ApJ, 927, 14
Chmyreva, E. G., Beskin, G. M., & Biryukov, A. V. 2010, AstL, 36, 116
Clegg, A. W., Fey, A. L., & Lazio, T. J. W. 1998, ApJ, 496, 253
Coles, W. A., Rickett, B. J., Gao, J. J., Hobbs, G., & Verbiest, J. P. W. 2010, ApJ, 717, 1206
Cordes, J. M. 1986, ApJ, 311, 183
Cordes, J. M., & Lazio, T. J. W. 2001, ApJ, 549, 997
Cordes, J. M., & Lazio, T. J. W. 2002, arXiv:astro-ph/0207156
Cordes, J. M., & Rickett, B. J. 1998, ApJ, 507, 846
Cordes, J. M., Rickett, B. J., Stinebring, D. R., & Coles, W. A. 2006, ApJ, 637, 346
Cordes, J. M., Weisberg, J. M., & Boriakoff, V. 1985, ApJ, 288, 221
Cordes, J. M., Weisberg, J. M., Frail, D. A., Spangler, S. R., & Ryan, M. 1991, Natur, 354, 121
Deller, A. T., Goss, W. M., Brisken, W. F., et al. 2019, ApJ, 875, 100
Donner, J. Y., Verbiest, J. P. W., Tiburzi, C., et al. 2019, A&A, 624, A22
Geyer, M., Karastergiou, A., Kondratiev, V. I., et al. 2017, MNRAS, 470, 2659
Goodman, J., & Narayan, R. 1985, MNRAS, 214, 519
Goodman, J. J., Romani, R. W., Blandford, R. D., & Narayan, R. 1987, MNRAS, 229, 73
Gupta, Y. 1995, ApJ, 451, 717
Gupta, Y., Rickett, B. J., & Lyne, A. G. 1994, MNRAS, 269, 1035
Gwinn, C. R. 2019, MNRAS, 486, 2809
Gwinn, C. R., & Sosenko, E. B. 2019, MNRAS, 489, 3692
Hewish, A. 1980, MNRAS, 192, 799
Hewish, A., Bell, S. J., Pilkington, J. D. H., Scott, P. F., & Collins, R. A. 1968, Natur, 217, 709
Hill, A. S., Stinebring, D. R., Asplund, C. T., et al. 2005, ApJL, 619, L171
Hill, A. S., Stinebring, D. R., Barnor, H. A., Berwick, D. E., & Webber, A. B. 2003, ApJ, 599, 457
Kuzmin, A. D., & Losovsky, B. Y. 2007, A&AT, 26, 597
Lambert, H. C., & Rickett, B. J. 1999, ApJ, 517, 299
Linsky, J. L., & Redfield, S. 2021, ApJ, 920, 75
Linsky, J. L., Redfield, S., & Tilipman, D. 2019, ApJ, 886, 41
Löhmer, O., Kramer, M., Mitra, D., Lorimer, D. R., & Lyne, A. G. 2001, ApJ, 562, L157
Main, R. A., Sanidas, S. A., Antoniadis, J., et al. 2020, MNRAS, 499, 1468
Mall, G., Main, R. A., Antoniadis, J., et al. 2022, MNRAS, 511, 1104
Manchester, R. N., Hobbs, G. B., Teoh, A., & Hobbs, M. 2005, AJ, 129, 1993
Marthi, V. R., Simard, D., Main, R. A., et al. 2021, MNRAS, 506, 5160
McKee, J. W., Zhu, H., Stinebring, D. R., & Cordes, J. M. 2022, ApJ, 927, 99
Michilli, D., Hessels, J. W. T., Donner, J. Y., et al. 2018, MNRAS, 476, 2704
Molnar, L. A., Mutel, R. L., Reid, M. J., & Johnston, K. J. 1995, ApJ, 438, 708
Ocker, S. K., Cordes, J. M., Chatterjee, S., & Dolch, T. 2021, ApJ, 922, 233
Pen, U.-L., & King, L. 2012, MNRAS Lett., 421, L132
Pen, U.-L., & Levin, Y. 2014, MNRAS, 442, 3338
Putney, M. L., & Stinebring, D. R. 2006, ChJAS, 6, 233
Ramachandran, R., Demorest, P., Backer, D. C., Cognard, I., & Lommen, A. 2006, ApJ, 645, 303
Reardon, D. J., Coles, W. A., Bailes, M., et al. 2020, ApJ, 904, 104
Rickett, B., Johnston, S., Tomlinson, T., & Reynolds, J. 2009, MNRAS, 395, 1391
Rickett, B., Stinebring, D., Coles, B., & Jian-Jian, G. 2011, in AIP Conf. Proc. 1357, RADIO PULSARS: AN ASTROPHYSICAL KEY TO UNLOCK THE SECRETS OF THE UNIVERSE, ed. M. Burgay et al. (Melville, NY: AIP), 97
Rickett, B. J. 1969, Natur, 221, 158
Rickett, B. J. 1970, MNRAS, 150, 67
Rickett, B. J. 1990, ARA&A, 28, 561
Rickett, B. J., Coles, W. A., Nava, C. F., et al. 2014, ApJ, 787, 161
Rickett, B. J., Lyne, A. G., & Gupta, Y. 1997, MNRAS, 287, 739
Rickett, B. J., Stinebring, D. R., Zhu, H., & Minter, A. H. 2021, ApJ, 907, 49
Romani, R. W., Narayan, R., & Blandford, R. 1986, MNRAS, 220, 19
Safutdinov, E. R., Popov, M. V., Gupta, Y., Mitra, D., & Kumar, U. 2017, ARep, 61, 406
Scheuer, P. A. G. 1968, Natur, 218, 920
Shi, X., & Xu, Z. 2021, MNRAS, 506, 6039
Simard, D., Pen, U. L., Marthi, V. R., & Brisken, W. 2019a, MNRAS, 488, 4952
Simard, D., Pen, U. L., Marthi, V. R., & Brisken, W. 2019b, MNRAS, 488, 4963
Spangler, S. R., & Gwinn, C. R. 1990, ApJL, 353, L29
Sprenger, T., Wucknitz, O., Main, R., Baker, D., & Brisken, W. 2021, MNRAS, 500, 1114
Sprenger, T., Main, R., Wucknitz, O., Mall, G., & Wu, J. 2022, MNRAS, 515, 6198
Stinebring, D. R., Hill, A. S., & Ransom, S. M. 2005, in ASP Conf. Ser. 328, Binary Radio Pulsars, ed. F. A. Rasio & I. H. Stairs (San Francisco, CA: ASP), 349
Stinebring, D. R., McLaughlin, M. A., Cordes, J. M., et al. 2001, ApJL, 549, L97
Stinebring, D. R., Rickett, B. J., & Ocker, S. K. 2019, ApJ, 870, 82
Sutton, J. M. 1971, MNRAS, 155, 51
Taylor, J. H., & Cordes, J. M. 1993, ApJ, 411, 674
Walker, M. A., Koopmans, L. V. E., Stinebring, D. R., & van Straten, W. 2008, MNRAS, 388, 1214
Walker, M. A., Melrose, D. B., Stinebring, D. R., & Zhang, C. M. 2004, MNRAS, 354, 43
Walker, M. A., & Stinebring, D. R. 2005, MNRAS, 362, 1279
Walker, M. A., Tuntsov, A. V., Bignall, H., et al. 2017, ApJ, 843, 15
Wang, N., Manchester, R. N., Johnston, S., et al. 2005, MNRAS, 358, 270
Wang, P. F., Han, J. L., Han, L., et al. 2018, A&A, 618, A186
Yao, J., Zhu, W., Manchester, R. N., et al. 2021, NatAs, 5, 788
Yao, J. M., Manchester, R. N., & Wang, N. 2017, ApJ, 835, 29
Zucker, C., Goodman, A. A., Alves, J., et al. 2022, Natur, 601, 334